

Infrared field compression

Liu An-Na^{1,2}, Liu Shu-Ning³, Jiao Shou-Zheng^{1,2}, Gao Wei⁴, Kang Qian-Long¹, Luo Min¹, Sun Hui-Ying⁵,
Cao Meng⁵, Ge Hao-Nan¹, Wang Fang¹, Wang Peng¹, Xie Run-Zhang^{1*}

1. State Key Laboratory of Infrared Physics, Shanghai Institute of Technical Physics, Chinese Academy of Sciences, Shanghai 200083, China;
2. University of Chinese Academy of Sciences, Beijing 100049, China;
3. Thrust of Microelectronics, Hong Kong University of Science and Technology (Guangzhou), Guangzhou 511453, China;
4. Shanghai Institute of Intelligent Science and Technology, Tongji University, Shanghai 200092, China;
5. School of Materials Science and Engineering, Shanghai University, Shanghai 200444, China)

Abstract: Infrared optical field compression provides an effective route to control mode dispersion and spatial distribution. In free space or homogeneous media, infrared propagating modes are diffraction-limited and difficult to achieve deep-subwavelength field compression. Optical field compression requires dispersion control and structure geometry design. In recent years, advances in low-dimensional materials and micro-nano fabrication broaden the physical implementation path of mode volume modulation. This review classifies infrared optical field into two fundamental types based on axial symmetry, including out-of-plane compression and in-plane compression. Out-of-plane compression forms normal (axial) compression states through interface dispersion and boundary conditions. Representative mechanisms include surface plasmon polaritons (SPPs), surface phonon polaritons (SPhPs), and waveguide modes. In-plane compression suppresses lateral propagation through disorder-induced interference, defect states, or geometric compression. This review compares physical origins and characteristic spatial scales of different mechanisms and summarizes research progress in infrared photodetection, surface-enhanced infrared absorption, and light-emission modulation. Further discussion examines the potential of hybrid in-plane-out-of-plane compression for enhancing optical field compression and tailoring mode distribution, and outlines future research directions.

Key words: photonic structures, micro-nano optics, mode volume compression, infrared detector, infrared light source

Introduction

Infrared optical field compression is an important research direction in photonics and quantum optics^[1,2]. It describes the spatial confinement of electromagnetic fields, typically accompanied by reduced mode volume and subwavelength field enhancement. The mode volume V_{mode} serves as a fundamental quantitative metric of confinement, characterizing the effective spatial extent of an optical mode and influencing the local density of optical states (LDOS), thereby governing light-matter interactions^[3]. In general, it can be expressed as

$$V_{\text{mode}} = \frac{\int \varepsilon(\mathbf{r}) |E(\mathbf{r})|^2 dV}{\max \left\{ \varepsilon(\mathbf{r}) |E(\mathbf{r})|^2 \right\}}, \quad (1)$$

where $E(\mathbf{r})$ represents the electric field distribution and $\varepsilon(\mathbf{r})$ is the dielectric permittivity. Reducing the mode volume concentrates optical energy into smaller spatial regions, thereby enhancing the sub-wavelength electric field intensity and strengthening light-matter interaction. Photonic structures capable of compressing optical modes into subwavelength volumes therefore provide effective pathways for infrared photodetection^[4], molecular sensing^[5,6], nonlinear optics^[7], and on-chip photonic integration^[8]. Infrared optical modes typically exhibit spatial scales comparable to their free-space wavelengths. Their wavevector distribution is constrained by the light cone and diffraction relations, making it difficult for homogeneous media to support high-momentum bound states or

Received date: 2026-03-19, **accepted date:** 2026-04-14

收稿日期: 2026-03-19, **录用日期:** 2026-04-14

Foundation items: Supported by the National Key Research and Development Program of China (2025YFF0520500); the National Natural Science Foundation of China (62522414, 62305359).

Biography: An-Na Liu (1998—), female, Jilin, Ph. D. Research focuses on infrared photonic structures. E-mail: liuanna@mail. sitp. ac. cn

* **Corresponding author:** E-mail: xierunzhang@mail. sitp. ac. cn

achieve deep subwavelength field compression^[9]. Therefore, structure geometry design becomes a central challenge in infrared photonics. In recent years, various physical platforms such as interfacial polaritons^[10], photonic bandgap structures^[11], and disordered scattering systems^[12] have been successively developed, achieving the redistribution of modal wavevectors across different axial symmetries. However, most studies classify optical field compression mechanisms by material or structural type. The systematic comparison based on different axial symmetries remains lacking. From the perspective of axial symmetry, infrared field compression can be classified into out-of-plane and in-plane types.

Out-of-plane confined optical modes are governed by interfacial dispersion or geometry along the axial direction. The mode exhibits exponential decay or forms confined eigenmode distributions along the axial direction, while remaining laterally propagating in-plane. Typical mechanisms include interfacial polariton bound states and waveguide cross-sectional confined modes^[13]. Their axial compression length can typically be confined to the subwavelength scale. In-plane compression corresponds to lateral compression within the structural plane. Representative mechanisms include Anderson localization (AL) induced by disorder-driven multiple scattering^[14], defect state compression in photonic bandgaps^[15], and SPPs field compression arising from geometric compression^[16]. The differences between the two mechanisms are reflected in the wavevector structure, the in-plane and out-of-plane compression lengths, and the effective mode-volume distribution.

In this review, we compare the in-plane and out-of-plane compression scales of plasmonic modes, phonon polaritons, waveguide modes, AL, bandgap defect states, and geometrically confined plasmons, as shown in Fig. 1. This comparison clarifies the differences in compression dimension, compression strength, and applicable regimes across distinct mechanisms. On this basis, coordinated design of axial and lateral compression enables hybrid in-plane and out-of-plane compression. Such hybrid compression further reduces mode volume and tailors the spatial distribution of modes, offering significant potential for nonlinear optical communication^[17], surface-enhanced infrared absorption (SEIRA)^[5], and light-emission modulation^[18]. By analyzing the physical origins and characteristic scales of mechanisms with different symmetries, this review provides a systematic framework for infrared light field regulation, encompassing in-plane, out-of-plane, and their hybrid compression.

1 Out-of-plane compression

Out-of-plane compression refers to electromagnetic modes that are strongly confined along the direction perpendicular to the structural surface (axial direction, typically defined as the z direction in extensive previous researches). This compression is governed either by the geometry along the axial direction or by the interplay between intrinsic material dispersion and interfacial condi-

tions. A common feature is that the electromagnetic field exhibits pronounced exponential decay or decays asymptotically faster than a polynomial law of r^{-2} along the axial direction. Typical out-of-plane compression mechanisms include surface plasmon polaritons (SPPs) compression, surface phonon polaritons (SPhPs) compression, and waveguide-mode compression. Among these mechanisms, SPPs provide extremely strong subwavelength confinement but suffer from significant Ohmic loss. SPhPs exhibit lower losses and higher quality factors in the infrared, though their operation bandwidth is limited by phonon resonances. Waveguide modes offer relatively low-loss confinement and good integration compatibility, but their compression strength is typically restricted by diffraction and refractive index contrast. These mechanisms therefore represent different routes for achieving axial electromagnetic confinement.

1.1 Surface plasmon polaritons (SPPs)

A SPPs is one of the most representative mechanisms for achieving out-of-plane infrared compression. SPPs are formed by the coupling between the collective oscillations of free electrons in metals (or metal-like materials) and electromagnetic waves. In the infrared spectral range, SPPs exhibit subwavelength compression, with fields decaying exponentially along the axial direction. The compression scale is determined by the complex dielectric function and dispersion relation, exhibiting as a mode characterized by in-plane propagation and out-of-plane compression.

For an ideal planar interface, the dispersion relation of SPPs can be written as^[19]

$$k_{SPP} = k_0 \sqrt{\frac{\varepsilon_m \varepsilon_d}{\varepsilon_m + \varepsilon_d}}, \quad (2)$$

here, ε_m and ε_d denote the complex dielectric permittivities of the metal and the dielectric, respectively. When $\text{Re}(\varepsilon_m) < -\varepsilon_d$, a bound interfacial mode can be supported. Because $|k_{SPP}| > k_0$, the mode lies outside the free-space light cone. This leads to an imaginary axial wavevector k_z , resulting in exponential decay perpendicular to the interface and subwavelength compression. The corresponding out-of-plane compression length is given by

$$\delta_{\perp} = \frac{1}{\text{Im}(k_z)}. \quad (3)$$

In the infrared regime, traditional SPPs exhibit long in-plane propagation lengths on the order of $L_{\parallel} \sim 10^2 \lambda_0$ with relatively weak axial compression ($\delta_{\perp} \sim 0.1-1 \lambda_0$)^[20]. The compression of the out-of-plane compression length confines the electromagnetic energy within a sub-wavelength region near the interface. This compression enhances the sub-wavelength electric field intensity and decreases the effective mode volume V_{eff} , thereby increasing the LDOS and strengthening light-matter interaction.

Because the resonance condition is governed by the in-plane wavevector through the SPPs dispersion relation, geometric parameters directly modulate the spectral position of the photo-response. Sobhani et al. employed a periodic gold grating-silicon Schottky architecture to control the plasmonic resonance through precise tuning of

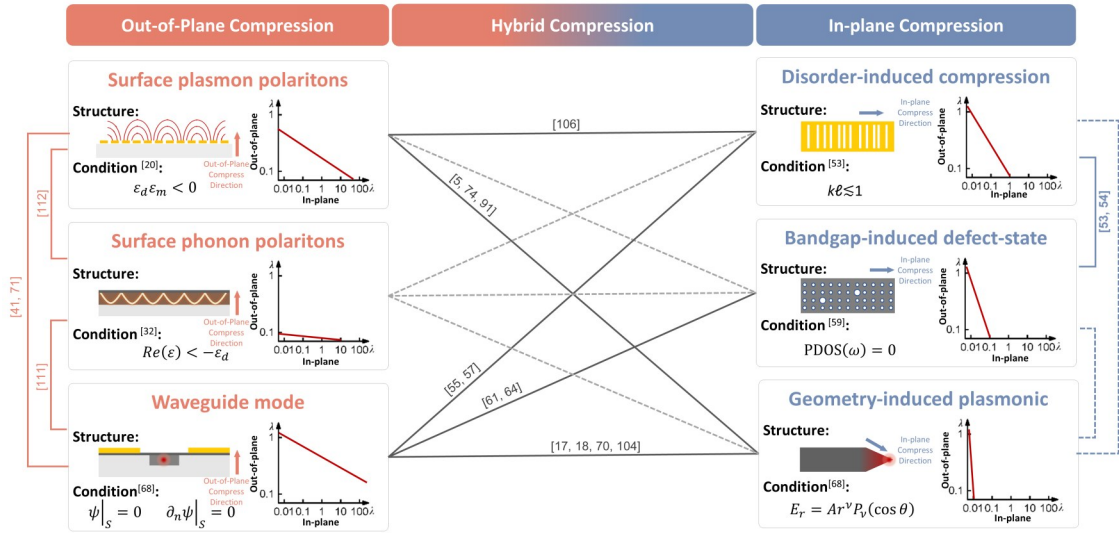


图1 红外光场压缩机制的概念示意图:包括面外压缩机制(表面等离激元(SPPs): $\varepsilon_d \varepsilon_m < 0$,即金属-介质界面两侧介电常数符号相反;表面声子极化激元(SPhPs): $Re(\varepsilon) < -\varepsilon_d$,即极性晶体中负介电响应支持表面束缚模;波导模式: $\psi|_s = 0$ 与 $\partial_n \psi|_s = 0$,由边界条件限定的受限本征模)。面内压缩机制包括(安德森局域: $kl \leq 1$,无序引起的多重散射抑制传播;缺陷态局域: ω 位于带隙内(光子态密度 PDOS = 0),通过带隙约束形成局域模;几何局域: $E_r = Ar^\nu P_\nu(\cos \theta)$,在尖锐边界附近($\nu < 0$)产生奇异场增强)。不同机制之间的连接表示潜在的耦合路径,其中实线表示本文讨论的物理耦合关系,虚线表示尚未展开但可能存在的耦合机制。

Fig. 1 Conceptual diagram of infrared field compression strategies: Including out-of-plane mechanisms (SPPs: $\varepsilon_d \varepsilon_m < 0$, opposite-sign permittivities at metal-dielectric interfaces; SPhPs: $Re(\varepsilon) < -\varepsilon_d$, negative permittivity in polar crystals enabling surface-bound modes; waveguides: $\psi|_s = 0$ and $\partial_n \psi|_s = 0$, boundary-defined confined eigenmodes). In-plane mechanisms include (Anderson localization: $kl \leq 1$, disorder-induced multiple scattering suppressing propagation; defect states: ω within bandgap (Photonic Density of States PDOS = 0), localized modes via bandgap confinement; geometric localization: $E_r = Ar^\nu P_\nu(\cos \theta)$, singular field enhancement near sharp boundaries with $\nu < 0$). Connections between mechanisms indicate possible coupling pathways. Solid lines indicate physically coupled mechanisms discussed in this work, while dashed lines denote potential couplings not covered here.

the grating period (Fig. 2a). The peak photo-response wavelength exhibited a linear dependence on the grating period, enabling narrowband spectral selectivity and deterministic wavelength tuning through structural design^[21]. In contrast, strongly confined SPPs platforms, such as graphene plasmons, metal-insulator-metal gap modes, and doped semiconductor plasmons, achieve deep subwavelength compression, reaching $\sim 0.1-1 \lambda_0$ in-plane and $\sim 0.01-0.1 \lambda_0$ out-of-plane compression^[22]. Fang et al. introduced metallic nanoantenna structures between bilayer graphene to excite out-of-plane confined SPPs modes at the metal-graphene interface. This structure enhanced the near-infrared photoresponse and achieved an internal quantum efficiency of up to 20% in the visible to near-infrared spectral range^[23]. Beyond near-field enhancement, SPPs can introduce polarization selectivity through geometric anisotropy. Wei et al. designed a T-shaped nanoantenna (Fig. 2b) and combined it with a Seebeck coefficient gradient to generate directional photocurrent, enabling a zero-bias mid-infrared graphene polarization photodetector^[24]. Building on this work, they further constructed a non-centrosymmetric nanoantenna structure using Ti and Pd in 2021^[25]. By tuning the antenna orientation, they reconfigured the con-

finned field distribution and achieved polarity-switchable photo-response through structural control (Fig. 2c). SPPs compression has also been widely employed in light-emission modulation^[26, 27], nonlinear optical enhancement^[28], surface-enhanced spectroscopy^[29] and photocatalysis^[30]. Further structural compression into nanocavities, nanogaps, or metal-insulator-metal (MIM) configurations enables simultaneous in-plane and out-of-plane compression. However, such strongly confined architectures are intrinsically limited by metallic Ohmic loss.

1.2 Surface Phonon polaritons (SPhPs)

Compared with SPPs, SPhPs provide another platform for out-of-plane compression of infrared electromagnetic fields. SPhPs originate from the coupling between electromagnetic fields and lattice vibrations (optical phonons) in polar crystals. In the infrared regime, metallic plasmons can provide strong field enhancement and reduced mode volume but are generally limited by Ohmic loss. In contrast, because the phonon damping rate is much smaller than the free-electron scattering rate, phonon polariton modes exhibit stronger optical compression, longer lifetimes, and lower loss. However, their operation is restricted to the Reststrahlen band of polar crystals, which limits the accessible spectral range and

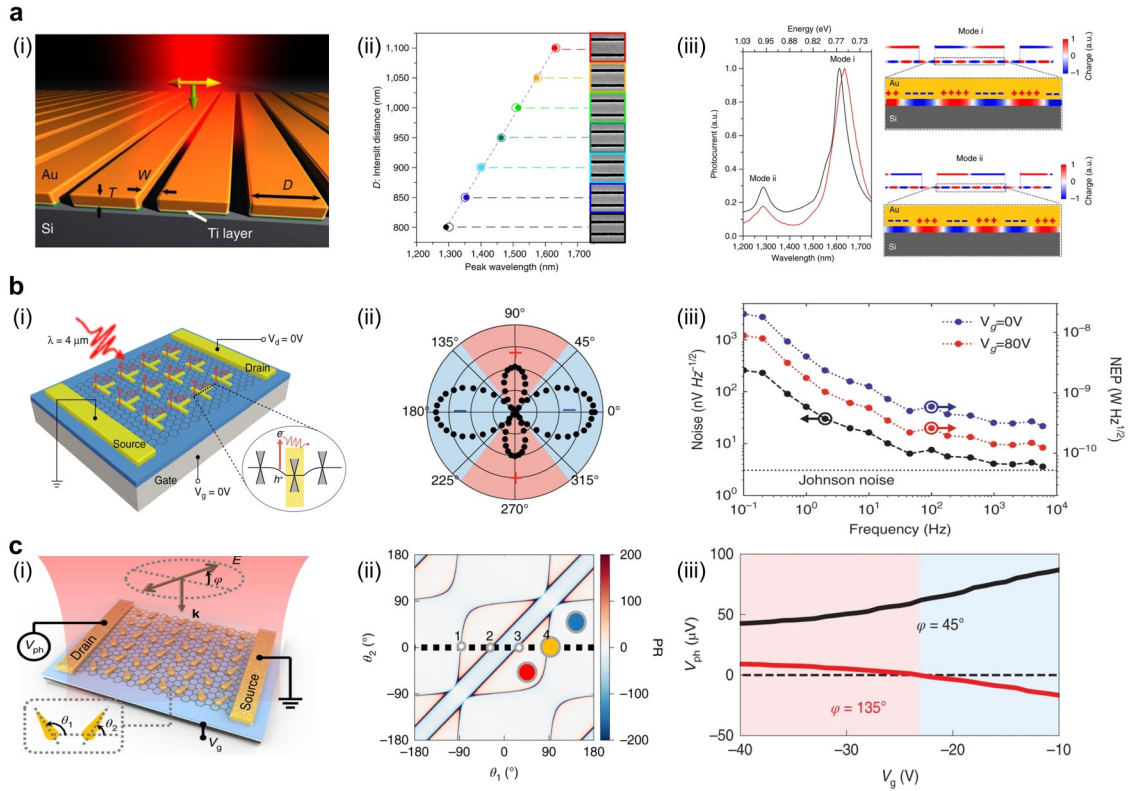


图2 具有面外压缩特性的SPPs结构:(a) (i) n型硅衬底上制备的金光栅结构示意图。(ii)在s偏振高斯光照射条件下($W = 250$ nm, $T = 200$ nm), 响应峰波长随狭缝间距呈线性变化关系。(iii)在实测响应谱中识别出的两种共振模式^[21]; (b) (i) T形超表面调控的石墨烯光探测器结构示意图($\lambda = 4 \mu\text{m}$)。 (ii)实测光电流 I_{ph} 的极坐标分布图, 表示其沿漏源电极方向的标量投影。(iii)实测的频率依赖噪声谱及计算得到的噪声等效功率(NEP)^[24]; (c) (i)纳米天线调控的半金属光探测器结构示意图。(ii)偏振比随纳米天线取向角(θ_1, θ_2)的变化关系。(iii)在偏振角 $\varphi = 45^\circ$ 和 135° 条件下测得的栅压依赖光电电压响应^[25]。

Fig. 2 SPPs structures with out-of-plane compression: (a) (i) Schematic of a gold grating patterned on an n-type silicon substrate. (ii) Linear dependence of the responsivity peak wavelength on slit spacing under s-polarized Gaussian illumination ($W = 250$ nm, $T = 200$ nm). (iii) Identification of two resonant modes in the measured responsivity spectra^[21]; (b) (i) Schematic of a T-shaped metasurface-mediated graphene photodetector ($\lambda = 4 \mu\text{m}$). (ii) Polar plot of the measured photocurrent I_{ph} , representing the scalar projection of I_{ph} along the drain-source electrode direction. (iii) Measured frequency-dependent noise spectrum and the calculated noise-equivalent power (NEP)^[24]; (c) (i) Schematic of a nanoantenna-mediated semimetal photodetector. (ii) Polarization ratio as a function of the nanoantenna orientation angles (θ_1, θ_2). (iii) Measured gate-voltage-dependent photovoltage at polarization angles $\varphi = 45^\circ$ and 135° ^[25].

material platforms. The dielectric response of such media can be expressed as^[31]

$$\varepsilon(\omega) = \varepsilon_{\infty, j} \left(1 + \frac{\omega_{LO, j}^2 - \omega_{TO, j}^2}{\omega_{TO, j}^2 - \omega^2 - i\omega\Gamma_j} \right), \quad (4)$$

here, ε_{∞} and Γ_j denote the high-frequency dielectric constant and the intrinsic damping coefficient of the material, respectively. The parameters $\omega_{LO, j}$ and $\omega_{TO, j}$ correspond to the longitudinal and transverse optical phonon frequencies that bound the Reststrahlen (RS) band along the principal direction j .

Typically, in the frequency range $\omega_{TO} < \omega < \omega_{LO}$, the real part of the dielectric function satisfies $\text{Re}(\varepsilon) < 0$, known as the Reststrahlen band. At an interface, the geometry requires continuity of the axial component of the electric displacement field. A bound interfacial mode can be supported at the interface if one medi-

um exhibits a negative dielectric response. The in-plane wavevector satisfies $k_{\parallel} > k_0$, and the field decays exponentially in the axial direction. The out-of-plane compression length δ_{\perp} is typically on the order of $0.1-1 \lambda_0$. Meanwhile, owing to the relatively low phonon damping, the in-plane propagation length can reach $L_{\parallel} \sim 10-100 \lambda_0$ (typically on the order of several tens of wavelengths)^[31, 32].

Early studies of SPHPs mainly focused on uniaxial crystals exhibiting out-of-plane hyperbolic dispersion. Within the Reststrahlen band of these materials, the in-plane and out-of-plane dielectric permittivities have opposite symbols, which supports volume-confined hyperbolic phonon polaritons, such as hBN^[31]. As research progressed, the concept of hyperbolic dispersion is extended from the out-of-plane direction to the in-plane direction. In 2018, Ma et al. showed that natural α -MoO₃ supports

out-of-plane compression and exhibits pronounced in-plane anisotropic dispersion^[33]. Infrared nano-imaging (Fig. 3a) directly visualized the elliptic and hyperbolic in-plane isofrequency contours of polaritons. The anisotropic dispersion enables directionally confined polariton propagation, leading to in-plane field compression and energy compression along specific crystallographic directions. Moreover, the long lifetime of phonon polaritons (~ 8 ps at room temperature) enables low-loss and long-range propagation. Zhao *et al.* further employed molybdenum isotope enrichment to suppress incoherent scattering caused by the natural multi-isotope distribution of Mo^[34], increasing the polariton lifetime to 13.9 ps with a propagation length of 6.76 μm (Fig. 3b). Controlling the atomic mass of Mo also provides an effective way to tune the polariton frequency in $\alpha\text{-MoO}_3$, offering a potential route toward ultra-low-loss polaritonic devices. Additionally, polar dielectric materials such as SiC support low-loss SPhPs in the mid-infrared regime, providing a representative platform for long-lived and highly confined polaritonic modes^[35].

Owing to their large in-plane momenta, SPhPs are generally difficult to couple to directly from free-space photons. Efficient excitation therefore often relies on momentum-matching schemes enabled by intense light sources, near-field probes, or photonic structures, which can limit practicality and overall coupling efficiency. Guo *et al.* exploited nonequilibrium carriers driven by a strong electrical bias, whose high-momentum near-field radiation can simultaneously satisfy energy and momentum matching with hyperbolic phonon polaritons in hBN^[36]. This mechanism enabled mid-infrared electroluminescence of polaritons without external optical coupling structures (Fig. 3c). The emission intensity can be further tuned by the applied bias through modifying the nonequilibrium carrier distribution and the tilted Fermi surface in graphene. In a related thermal excitation, Hutchins *et al.* showed that hot nonequilibrium electrons at Au/hBN interface can excite volume-confined hyperbolic phonon polaritons in hBN via near-field radiation, leading to ultrafast (picosecond-scale) interfacial heat transport (Fig. 3d)^[37]. Coupling SPhPs with photonic crystals, metasurfaces, or defect states can generate confined polaritonic modes, enabling simultaneous in-plane and out-of-plane compression^[38].

1.3 Waveguides

In dielectric or metallic waveguides, guided modes are supported when the propagation constant satisfies $n_{\text{clad}}k_0 < \beta < n_{\text{core}}k_0$. Under this condition, the electromagnetic field decays evanescently along the direction axial to the interface while propagating within the interface plane. In infrared dielectric waveguides, the out-of-plane compression length is typically on the order of $1\lambda_0$. Such compression enables light to be concentrated within a wavelength-scale cross section while maintaining extended propagation along the interface, thereby allowing precise control of modal distribution, interaction length, and coupling to active materials. Consequently, waveguide structures constitute a fundamental platform

for integrated infrared photonics and for engineering light-matter interactions.

In the field of photodetection, early work introduced a graphene onto a silicon optical waveguide on a silicon-on-insulator (SOI) (Fig. 4a) to realize evanescent-field coupling absorption. A responsivity of 0.13 A W^{-1} was achieved at 2.75 μm , demonstrating the effectiveness of waveguide-enhanced absorption^[39]. In the same year, Gan *et al.* employed an asymmetric metal-doped graphene junction to decouple the optical absorption path from the carrier transport path (Fig. 4b), achieving a response speed exceeding 20 GHz under zero bias^[40]. In 2020, Guo *et al.* designed an ultrathin wide-ridge silicon-graphene hybrid plasmonic waveguide. The modal field distribution was optimized to enhance graphene absorption and suppress metal loss. The device achieved a responsivity of 0.4 A W^{-1} and a 3 dB bandwidth exceeding 40 GHz at 1.55 μm (Fig. 4c). This result demonstrates the coexistence of high responsivity and high-speed operation under low bias^[41]. Flöry *et al.* integrated a vertical MoTe_2 -graphene heterojunction onto a silicon waveguide, orienting the carrier transport path perpendicular to the optical propagation direction (Fig. 4d). This design increased the bandwidth of the TMDC photodetector to 24 GHz^[42].

In electro-optic modulation, dispersion engineering and traveling-wave electrode design based on thin-film lithium niobate enabled ultra-broadband high-speed modulation covering the O-U bands and extending to the 2 μm band (Fig. 4e). The devices achieved a 3 dB bandwidth of ~ 100 GHz in the O-S-C-L bands, and more than 50 GHz at 2 μm , demonstrating continuous operation across multiple wavelength bands^[43]. In nonlinear optics, the compression of modal area in waveguides increases the effective nonlinear coefficient and enhances the efficiency of third-order nonlinear interactions. Kuyken *et al.* generated an octave-spanning mid-infrared frequency comb covering 1500-3300 nm in a silicon nanowire waveguide using 16 pJ pulse energy (Fig. 4f) and verified its phase coherence^[44]. In addition, semiconductor waveguide structures based on the free-carrier response of two-dimensional materials^[45] or longitudinal bulk plasmon modes in heavily doped semiconductors introduce strong electronic nonlinearity into guided-mode systems^[46]. These platforms enhance the effective nonlinear coefficient while maintaining propagation lengths on the order of hundreds of micrometers, providing a physical foundation for high-performance and multifunctional integrated infrared optoelectronic devices. Hu *et al.* integrated photoconverting materials with dielectric waveguides, demonstrating on-chip optoelectronic logic gates operating in the telecom band^[47]. By exploiting the strong optical confinement provided by the waveguide together with the built-in electric field in the photodetector, efficient compression of the optical field and high-efficiency extraction of the photoelectric signal were achieved, enabling on-chip optoelectronic logic operations in the telecom band.

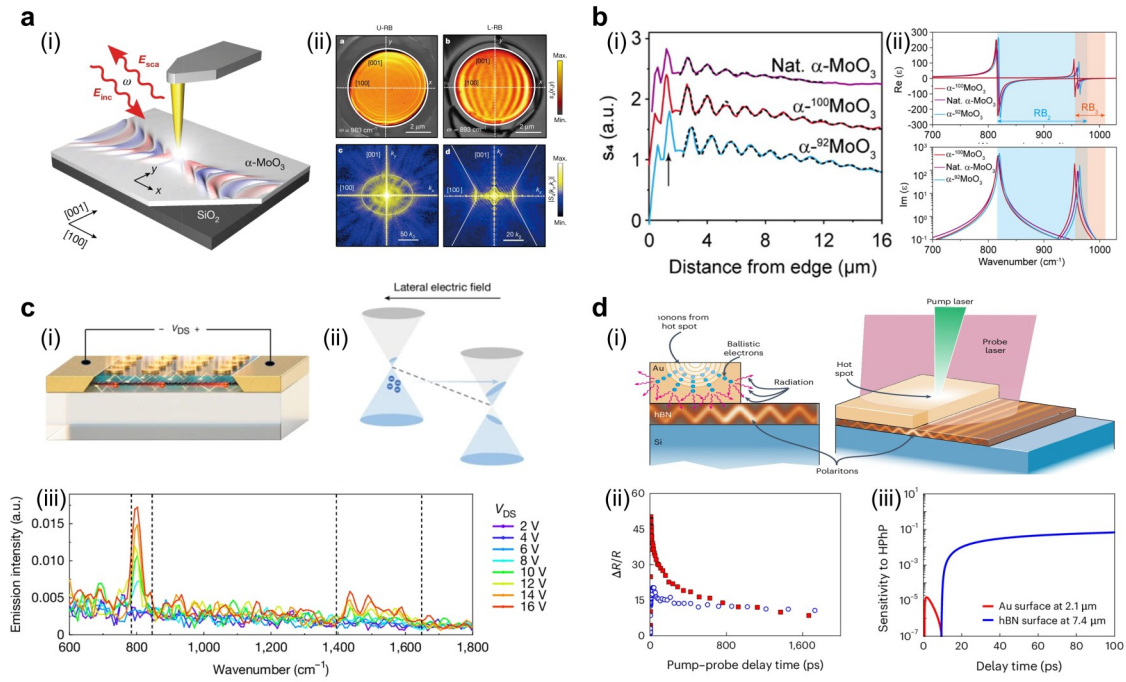


图3 具有面外压缩特性的SPhPs结构:(a) (i)用于成像面内双曲材料 α -MoO₃的s-SNOM实验装置示意图。(ii) α -MoO₃薄片的近场振幅图 S_4 及其对应的椭圆型与双曲型色散等频轮廓($\omega_u = 983 \text{ cm}^{-1}$, $\omega_l = 893 \text{ cm}^{-1}$)^[33];(b) (i)沿[100]方向提取的表面声子极化激元近场分布曲线。(ii)不同同位素富集条件下 α -MoO₃的介电函数实部与虚部^[34];(c) (i)hBN/graphene/hBN范德华异质结构中声子极化激元电致发光示意图。(ii)横向电场作用下石墨烯中的Zener-Klein隧穿与费米面倾斜。(iii)声子极化激元电致发光光谱随源漏偏压 V_{DS} 的变化关系($T = 83 \text{ K}$)^[36];(d) (i)基于双曲声子极化激元介导的泵浦-探测测量示意图($\lambda_{\text{pump}} = 520 \text{ nm}$, intensity $> 0.3 \text{ GW m}^{-2}$)。(ii)Au在Si和hBN衬底上的实测热反射信号。(iii)双曲声子极化激元界面耦合的相对灵敏度^[37]。

Fig. 3 SPhPs with out-of-plane compression: (a) (i) Schematic of the s-SNOM experimental setup used to image the in-plane hyperbolic material α -MoO₃. (ii) Near-field amplitude image S_4 of α -MoO₃ flake and the corresponding elliptic and hyperbolic dispersion contours ($\omega_u = 983 \text{ cm}^{-1}$, $\omega_l = 893 \text{ cm}^{-1}$)^[33]; (b) (i) Near-field profiles of SPhPs extracted along the [100] direction. (ii) Real and imaginary parts of the dielectric function for α -MoO₃ with different isotope enrichments^[34]; (c) (i) Schematic of PhP electroluminescence in an hBN/graphene/hBN van der Waals heterostructure. (ii) Zener-Klein tunnelling and Fermi-surface tilting in graphene under a lateral electric field. (iii) PhP electroluminescence spectra as a function of the source-drain bias voltage V_{DS} ($T = 83 \text{ K}$)^[36]; (d) (i) Schematic of the pump - probe measurement mediated by hyperbolic phonon polaritons ($\lambda_{\text{pump}} = 520 \text{ nm}$, intensity $> 0.3 \text{ GW m}^{-2}$). (ii) Measured thermoreflectance signals for Au on Si and hBN substrates. (iii) Relative sensitivity of HPhP interfacial coupling^[37].

2 In-plane compression

In-plane compression refers to the lateral compression of electromagnetic energy within the structural plane, perpendicular to axial direction and lying in the x - y direction, as commonly defined in previous studies. Its physical origin lies in restricting the propagation degrees of freedom of electromagnetic waves in the plane, thereby confining optical energy to confined regions. Typical mechanisms for in-plane compression include disorder-induced AL, bandgap-induced defect-state compression, and geometry-induced compression. In these systems, modes that axially propagate along an interface become confined within a finite region, forming spatially confined optical modes. Such confined modes typically exhibit strong field enhancement and frequency selectivity, enabling high-Q optical microcavities, low-threshold lasing, and high-density photonic integration.

2.1 Disorder-induced Anderson compression

AL was first proposed by Anderson in 1958 in electronic transport systems^[48], describing the transition of electron wavefunctions from extended states to spatially confined states in a disordered potential. Subsequent theoretical and experimental studies confirm that this mechanism reflects a universal wave phenomenon and can be extended to classical wave systems such as photons and acoustic waves^[49-51]. In optical systems, refractive-index fluctuations or structural randomness can act as an effective disordered potential. During multiple random scattering events, coherent interference occurs. At the Ioffe-Regel condition $kl \sim 1$, in-plane propagating modes evolve into exponentially decaying confined modes. The key physical parameters describing this process are the compression length ξ and the transport mean free path l .

In 2005, Bertolotti et al. observed Anderson-confined modes in a one-dimensional disordered system

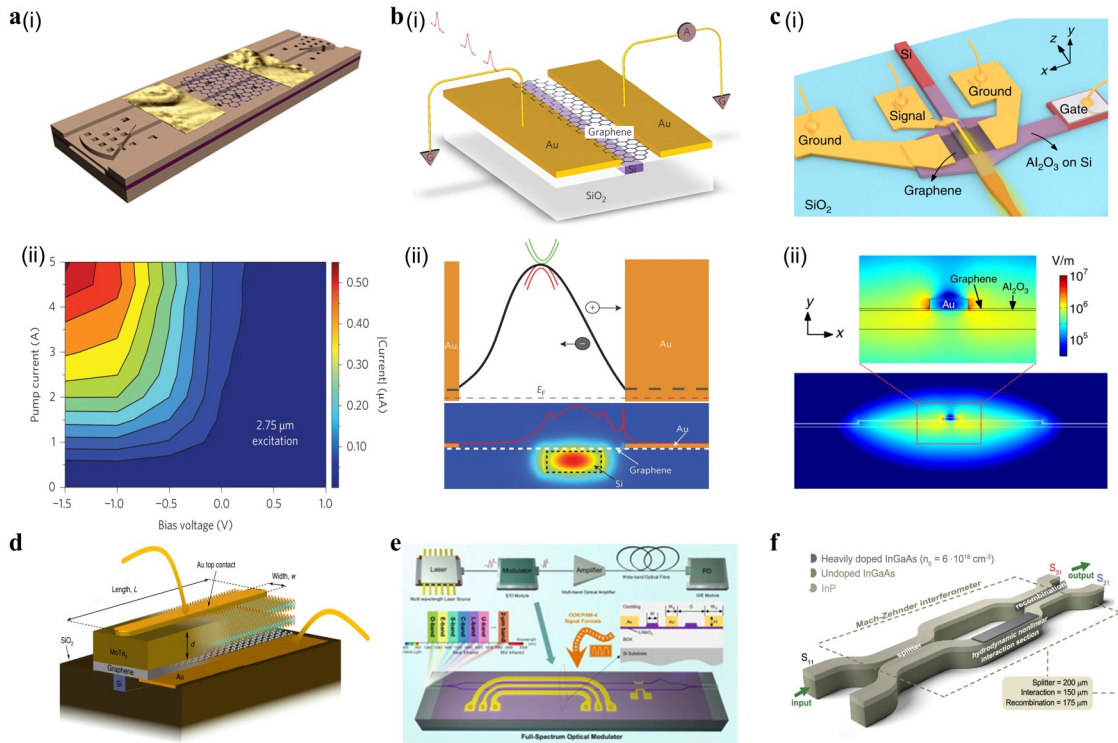


图4 具有面外压缩特性的波导结构:(a) (i)石墨烯-硅异质结构波导光探测器示意图。(ii)在($\lambda = 2.75 \mu\text{m}$)条件下,电流随入射光泵浦功率及外加偏压的变化关系^[39]; (b) (i)波导集成石墨烯光探测器结构示意图。(ii)石墨烯沟道中的电势分布及电场仿真结果^[40]; (c) (i)硅-石墨烯混合等离子激元波导光探测器结构。(ii)准TE₀模式的电场分布($\lambda = 2 \mu\text{m}$)^[41]; (d)垂直结构MoTe₂-石墨烯异质结光探测器^[42]; (e)面向扩展全光谱光通信系统的宽带薄膜铌酸锂光调制器^[43]; (f)基于高非线性波导的马赫-曾德干涉仪全光调制示意图^[44]。

Fig. 4 Waveguides with out-of-plane compression. a, (i) Schematic of a graphene-silicon heterostructure waveguide photodetector. (ii) Current as a function of incident optical pump current and electric bias voltage ($\lambda = 2.75 \mu\text{m}$)^[39]. b, (i) Schematic of a waveguide-integrated graphene photodetector. (ii) Potential profile and simulated electric field in the graphene channel^[40]. c, (i) Structure of a silicon-graphene hybrid plasmonic waveguide photodetector. (ii) Electric-field distribution of the quasi-TE₀ mode ($\lambda = 2 \mu\text{m}$)^[41]. d, Vertical MoTe₂-graphene heterostructure photodetector^[42]. e, Broadband thin-film lithium niobate optical modulator for an extended full-spectrum optical communication system^[43]. f, Schematic of all-optical modulation in a Mach-Zehnder interferometer based on a highly nonlinear waveguide^[44].

(Fig. 5a). These modes appeared as narrow high-transmission peaks in the transmission spectrum T . The averaged logarithmic transmission $\ln T$ decayed linearly with sample thickness, directly reflecting exponential spatial attenuation with a compression length of approximately $15 \mu\text{m}$ ^[52]. In addition, extended multi-resonant modes, known as necklace states, were observed in the system, revealing the coexistence of compressed and extended modes in disordered media. In two-dimensional photonic lattices, Schwartz *et al.* introduced controllable disorder using an optical induction technique (Fig. 5b). As the disorder strength increased, the output intensity profile of the lattice evolved from a Gaussian distribution characteristic of diffusion to an exponentially decaying profile associated with compression behavior. This transition reveals the evolution of transport from ballistic transport to diffusive transport and eventually to AL^[53]. In quasiperiodic photonic systems, transport behavior ex-

hibited a more complex response to disorder (Fig. 5c). Moderate disorder enhanced wave-packet spreading within certain band regions, while further increasing disorder intensity leads to the occurrence of AL^[54]. This behavior arises from the interplay between critical states in quasiperiodic systems and disorder-induced scattering. Beyond fundamental studies of AL, optical AL has also shown potential applications in random lasers^[55, 56] and optical fiber transmission. Karbasi *et al.* demonstrated image transport in polymer disordered fibers based on transverse AL^[57]. The fiber consists of randomly stacked PMMA and PS strands with different refractive indices. The transverse refractive-index fluctuations induce AL and form stable confined transport channels within the fiber core. As a result, transverse crosstalk is suppressed, enabling low pixelation and high-contrast imaging (Fig. 5d). The imaging performance is comparable to that of commercial multicore imaging fibers, demon-

strating the potential of AL for optical information transmission. Ng et al. further introduced AL into the field of cavity optomechanics (Fig. 5e). In an air-slot photonic crystal waveguide, Anderson-localized modes induced by sidewall roughness exhibit a quality factor Q as high as 2.8×10^5 and a mode volume below the diffraction limit. These modes couple to mechanical modes with a strength exceeding 200 kHz, enabling self-sustained oscillations. This system provides a new platform for exploring optomechanical effects in multiple-scattering systems^[58].

2.2 Bandgap-induced defect-state compression

In periodic photonic crystals, the existence of a pho-

tonic bandgap prevents the propagation of light within a specific frequency range inside the crystal. Perturbation of the perfect periodic photonic crystals, for example by removing a dielectric rod or modifying an air hole, introduces discrete defect modes within the bandgap^[9, 59]. The frequencies of these defect modes lie inside the bandgap, and the corresponding optical fields are strongly confined around the defect region, forming a high- Q optical microcavity (Fig. 6a). The compression typically occurs on a deeply subwavelength scale in the plane, with an in-plane compression length on the order of $\sim 0.1 \lambda_0$, while the out-of-plane compression length remains on the order

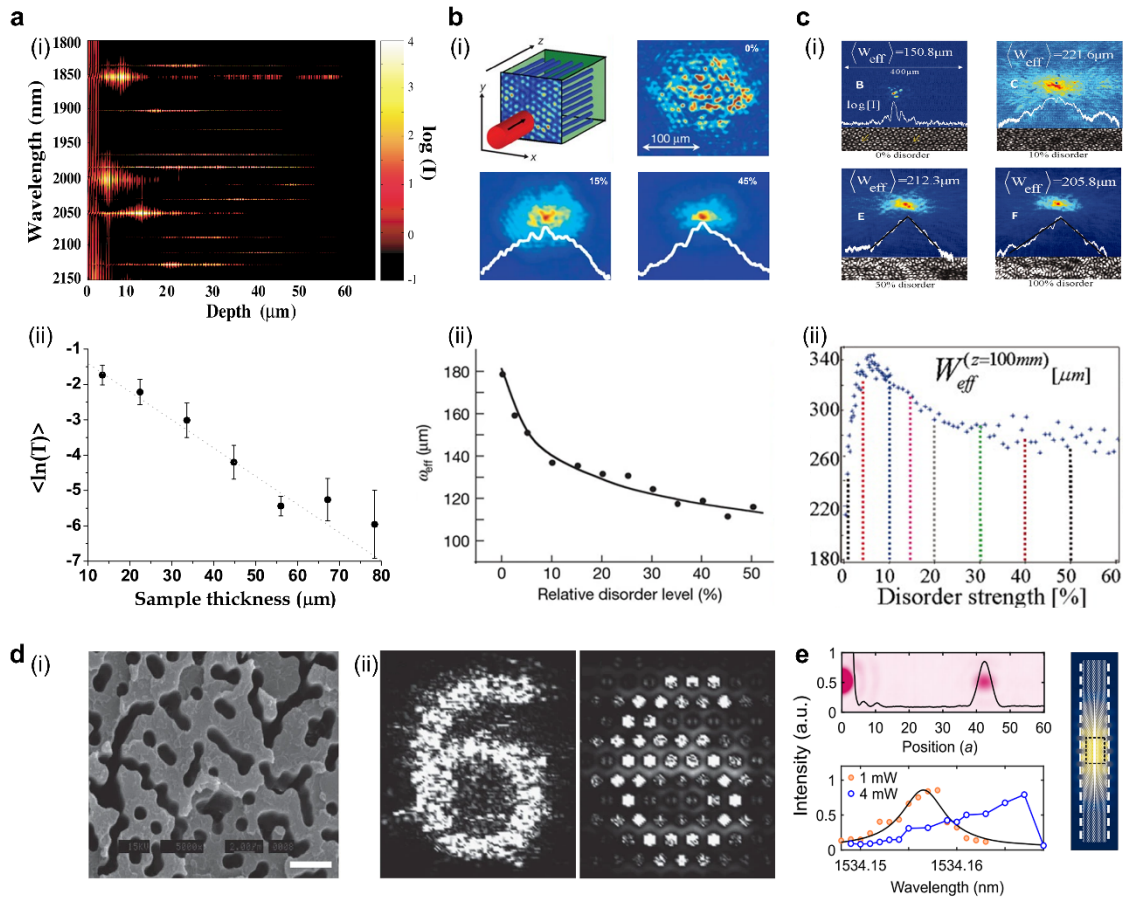


图5 无序诱导的安德森局域:(a) (i)样品内部的计算强度分布。(ii)无序体系中透射随样品厚度呈指数衰减关系^[52];(b) (i)在0%、15%和45%无序度条件下晶格输出强度分布的实验测量结果($\lambda = 514 \text{ nm}$, $\text{FWHM} = 10.5 \mu\text{m}$)。(ii)晶格输出端的集合平均有效宽度随无序度变化关系^[53];(c) (i)传播距离 $z = 10 \text{ mm}$ 后的集合平均输出强度实验结果。(ii)准晶结构中平均光束宽度随无序强度的变化关系^[54]。(d) (i)无序光纤的扫描电子显微镜(SEM)图像。(ii)对应的传输成像结果,并与FIGH-10-350S成像光纤进行对比($\lambda = 405 \text{ nm}$)^[57];(e)安德森局域腔模的空间分辨及远场光谱分辨表征结果,以及对应的SLN腔内本征力学模^[58]。

Fig. 5 Disorder-induced Anderson localization. (a) (i) Calculated intensity distribution inside the sample. (ii) Exponential decay of transmission with sample thickness in a disordered system^[52]; (b) (i) Experimentally measured output intensity distributions of the lattice for 0%, 15%, and 45% disorder levels ($\lambda = 514 \text{ nm}$, $\text{FWHM} = 10.5 \mu\text{m}$). (ii) Ensemble-averaged effective width measured at the lattice output as a function of disorder level^[53]; (c) (i) Experimental results showing the ensemble-averaged output intensity after ($z = 10 \text{ mm}$). (ii) Average beam width in a quasicrystal as a function of disorder strength^[54]; (d) (i) SEM image of the disordered fibres. (ii) The corresponding transmitted image compared with a FIGH-10-350S imaging fiber ($\lambda = 405 \text{ nm}$)^[57]; (e) Spatially resolved and far-field spectrally resolved characterization of Anderson-localized cavity modes, together with the fundamental in-plane mechanical mode of the SLN cavity^[58].

of $\sim 1 \lambda_0$ ^[60]. Defect modes are equivalent to discrete confined energy levels introduced into the bandgap where light propagation is otherwise forbidden, enabling the trapping, compression, and selective radiation of photons at specific frequencies. Unlike Anderson compression, defect-state compression arising from a photonic bandgap exhibits higher determinism and design flexibility. The spatial position, resonance frequency, and even the modal field distribution can be precisely controlled through geometric engineering of the defect structure.

Early studies mainly focused on point-defect cavities in two-dimensional photonic crystal slabs. Painter *et al.* first constructed a defect cavity in a two-dimensional photonic crystal by removing a single air hole and demonstrated single-defect-mode lasing under optical pumping. The cavity exhibited a small mode volume of approximately $0.03 \mu\text{m}^3$, revealing the strong potential of photonic crystal defect cavities for strong optical compression^[15]. Subsequently, Akahane *et al.* introduced fine positional modulation of the air holes around the defect cavity, shaping the cavity-mode envelope into a Gaussian profile and thereby suppressing the coupling of high-spatial-frequency components in k -space to radiation modes. (Fig. 6b). The quality factor of the defect cavity in a silicon two-dimensional photonic crystal slab increased from several hundred to 45,000, while maintaining a very small mode volume ($V=0.07 \mu\text{m}^3$)^[60]. Subsequent studies further pushed the quality factor Q of photonic crystal defect cavities to new levels. The Noda group introduced a heterostructure cavity in two-dimensional photonic crystals by connecting regions with different lattice constants, creating a cavity with smoother longitudinal compression of the optical field (Fig. 6c). This design increased the Q factor to the million range^[61]. A higher Q/V ratio enables stronger field enhancement and longer cavity-mode lifetimes within a small mode volume, thereby significantly strengthening the coupling between the cavity field and emitters. By embedding emitters such as quantum dots into photonic crystal defect cavities, researchers observed an enhancement of the spontaneous emission rate induced by the Purcell effect^[62]. In the strong-coupling regime, vacuum Rabi splitting appears, indicating coherent and reversible energy exchange between the exciton and the cavity mode (Fig. 6d)^[63].

In recent years, research on bandgap-confined defect states has gradually extended beyond the conventional photonic bandgap framework, giving rise to several new compression mechanisms. Sang Soon Noh and co-workers proposed and experimentally demonstrated a bandgap-center defect state protected by a topological invariant^[64]. This structure is based on a two-dimensional photonic crystal with C_6 symmetry, in which a topological phase transition is induced by tuning the intra-cell and inter-cell coupling strengths. A zero-dimensional corner-state defect mode emerges at the center of the bandgap (Fig. 6e), providing a new route for the robust control of defect-mode frequency and spatial compression. Zhu *et al.* introduced a topological lattice defect into the cross-section of a photonic crystal fiber, thereby realizing a

guided topological defect mode (Fig. 6f). Topological photonic crystal fiber exhibits lower transmission loss under bending conditions compared with conventional solid-core photonic crystal fibers^[65]. In addition, Rong *et al.* proposed a Berry-phase defect photonic crystal by embedding anisotropic nanoantennas with continuously varying orientations into a photonic crystal slab, thereby forming a near-field Berry-phase defect mode^[66]. This mode enables spatial control of the geometric phase of the emitted polarization field. Thence, valley excitons in monolayer WSe_2 or quantum dots can acquire spin-dependent phase encoding. Based on this mechanism, a photon Rashba-type dispersion splitting associated with the valley degree of freedom was experimentally observed. This work highlights the potential of topological defect engineering for controlling quantum light sources. Notably, recent studies show that optical mode volume compression can also occur without a photonic bandgap. By introducing symmetry mismatch, compression can emerge through bound states in the continuum (BICs). Vaidya *et al.* proposed and experimentally demonstrated a point-defect BIC in a two-dimensional photonic crystal^[67]. The mode exhibits exponential decay at the defect position, providing an additional physical route for realizing optical compression.

Over the past two decades, defect cavities have achieved significant performance improvements through increasingly precise control of band structures and confined optical fields, including boundary engineering and heterostructure design. These advances have enabled the development of core devices including ultra-compact lasers and efficient single-photon sources. In the future, on-chip integration of high-performance defect cavities with active gain media and emerging two-dimensional materials will play an important role, particularly for applications in quantum light sources, nonlinear optics, and spin-related photonics.

2.3 Geometry-induced compression

Geometry-induced compression originates from strong surface charge accumulation at high-curvature geometric features, such as tips, edges, and nanogaps. In plasmonic structures with gradually varying geometry, the process typically follows adiabatic compression. The slow structural variation allows the structure to be approximated locally as uniform regions with nearly parallel boundaries. The mode therefore evolves gradually along the structure, enabling adiabatic nanofocusing while suppressing radiation loss^[68]. In metallic nanostructures with characteristic dimensions much smaller than the incident wavelength, geometric boundaries strongly confine the collective oscillation of conduction electrons. This compression compresses electromagnetic energy into deep-subwavelength hot spots beyond the diffraction limit. In such structures, the in-plane compression length can reach the order of $10^2 \lambda_0$, while the out-of-plane decay length is typically on the order of $1 \lambda_0$. Typical manifestations include tip enhancement at sharp tips or edges and gap plasmon hot spots in nanoscale gaps^[69]. The former mainly arises from geometric field concentration (the lightning-rod effect) and typically exhibits broadband en-

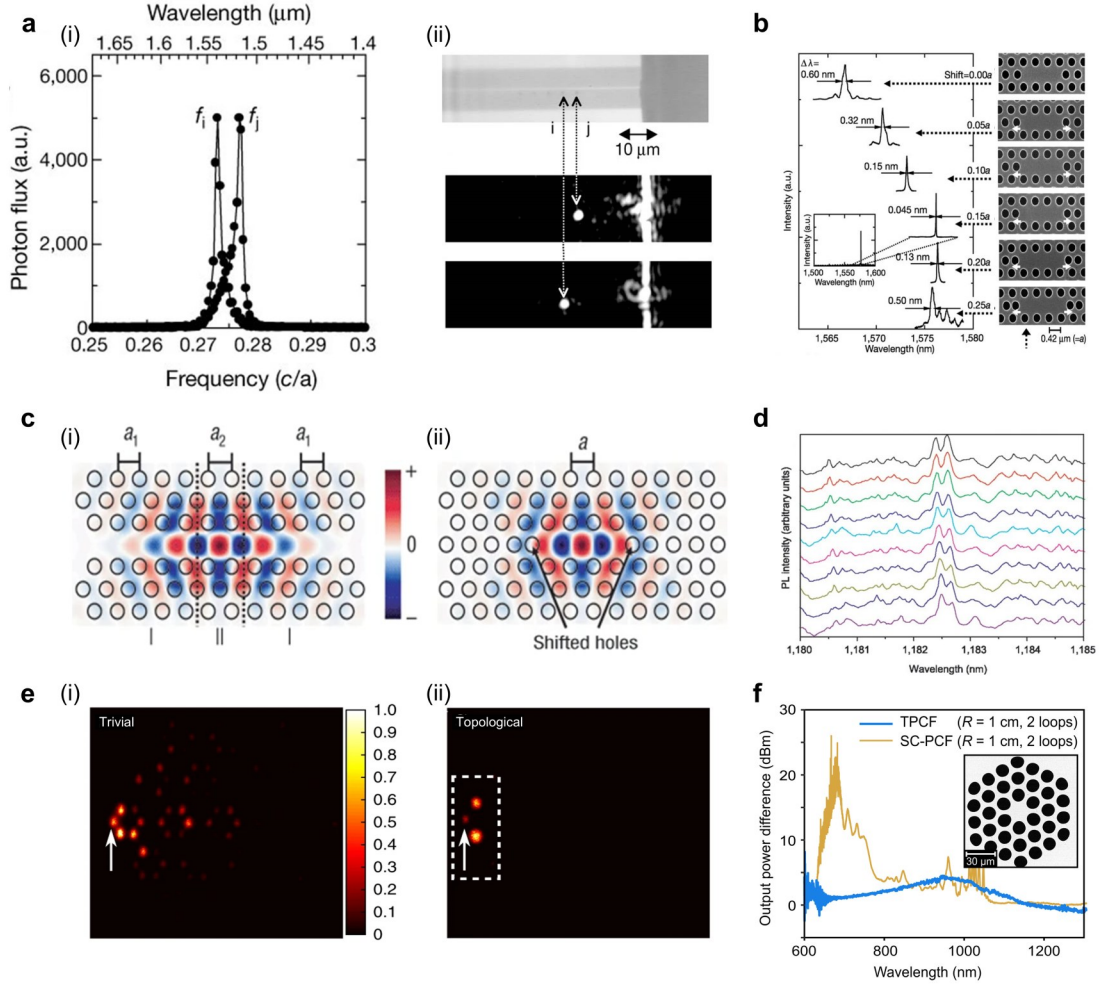


图6 带隙诱导的缺陷态压缩:(a) (i)光子晶体中的两个孤立缺陷可俘获并发射光子,在光谱中产生离散的高Q共振峰($\lambda_i = 1.566 \mu\text{m}$, $\lambda_j = 1.545 \mu\text{m}$)。 (ii)红外相机观测到的受限辐射图像,显示缺陷模的空间压缩特性^[59]; (b)二维光子晶体中由不同空气孔位移形成的腔体共振光谱及其对应的扫描电子显微镜(SEM)图像^[60]; (c) (i)双异质结构光子晶体腔的电场分布。(ii)由三个缺失空气孔形成的点缺陷腔的电场分布($a = 420 \text{ nm}$)^[61]; (d)近零失谐光致发光PL光谱呈现双峰发射特征,表明量子点-纳米腔体系中的真空Rabi劈裂现象($T = 15\text{-}19.5 \text{ K}$, 间隔 0.5 K ; $P = 0.78 \mu\text{W}$; 积分时间 $t = 60 \text{ s}$)^[63]; (e) (i)平庸相与(ii)拓扑相的衍射输出强度分布对比,其中拓扑相表现出角态局域模式^[64]; (f)拓扑光子晶体光纤(TPCF)与实心芯光子晶体光纤(SC-PCF)在直波导与弯曲波导($R = 1 \text{ cm}$)条件下的输出功率差异。插图为SC-PCF的SEM图像^[65]。

Fig. 6 Bandgap-induced defect-state compression: (a) (i) Two isolated defects in a photonic crystal capture and emit photons, producing discrete high-Q resonant peaks in the spectrum ($\lambda_i = 1.566 \mu\text{m}$, $\lambda_j = 1.545 \mu\text{m}$). (ii) Confined radiation image observed by an infrared camera, showing the spatial compression of the defect mode^[59]; (b) Resonant spectra of cavities formed by different air-hole displacements in a two-dimensional photonic crystal and their corresponding SEM images^[60]; (c) (i) Electric-field distribution of a double-heterostructure photonic crystal cavity. (ii) Electric-field distribution of a point-defect cavity formed by three missing air holes ($a = 420 \text{ nm}$)^[61]. d, Near-zero-detuning photoluminescence (PL) spectra showing double-peaked emission, indicating dot - nanocavity vacuum Rabi splitting ($T = 15\text{-}19.5 \text{ K}$, step 0.5 K ; $P = 0.78 \mu\text{W}$; integration time $t = 60 \text{ s}$)^[63]; (e) Comparison of diffracted output intensity distributions for (i) the trivial phase and (ii) the topological phase, where the topological phase exhibits corner-confined modes^[64]; (f) Output power difference between straight and bent fibers ($R = 1 \text{ cm}$) for the topological photonic crystal fiber (TPCF) and the solid-core photonic crystal fiber (SC-PCF). Inset: SEM image of SC-PCF^[65].

hancement. The latter originates from gap plasmon resonance and produces strong, spectrally narrow confined field enhancement near specific wavelengths.

Tapered structures represent a typical platform for geometrically induced plasmon compression. Stockman

theoretically predicted this adiabatic nanofocusing effect. As SPPs propagate toward the tip, both the group velocity and phase velocity gradually decrease and approach zero, leading to energy accumulation at the apex and the formation of field enhancement. The key require-

ment is that the geometric variation of the taper is sufficiently smooth to satisfy the adiabatic condition^[14]. Subsequently, Verhagen *et al.* experimentally observed plasmon focusing in a tapered silver waveguide (Fig. 7a). The near-field distribution was visualized via upconversion luminescence from erbium ions, demonstrating the capability of the tapered structure to spatially compress infrared plasmons^[18]. Schnell *et al.* further extended this concept to the mid-infrared regime, employing a tapered two-wire transmission line to achieve extreme field compression down to $\lambda/150 \approx 60$ nm ($\lambda = 9.3$ μm) (Fig. 7b)^[70].

Furthermore, resonant coupling between tapered structures and nanoscale gaps enables adiabatic nanofocusing of energy into the gap region, yielding stronger compression than isolated nanogaps. Choo *et al.* designed a three-dimensionally tapered-gap waveguide based on an MIM structure (Fig. 7c). By simultaneously reducing the gap width and the metal waveguide width, the structure compresses an incident 830 nm optical field into a region of approximately 14×80 nm², producing an intensity enhancement of about 400 times^[71]. Zenin *et al.* further combined tapered nanofocusing with a gap antenna, achieving extreme field enhancement of approximately 12000 within the nanogap region, with the confined field confined to a volume of about $30 \times 30 \times 10$ nm³ (Fig. 7d). This configuration provides an ideal platform for on-chip nonlinear optics^[72]. For integrated photonic applications, hybrid waveguide architectures offer an effective route to combine strong compression with low-loss propagation. Nielsen *et al.* realized a hybrid plasmonic waveguide on a silicon-on-insulator platform. Free-space light was efficiently coupled into a silicon waveguide using a curved grating coupler. The guided energy was adiabatically compressed by a tapered metallic structure into a 20 nm nanogap, resulting in more than 400-fold field enhancement and coupling efficiencies approaching 80%^[73]. By combining the low-loss transport of silicon photonics with the deep-subwavelength compression of plasmonics, this architecture provides a promising platform for on-chip optical interconnects, electro-optic modulation, and nonlinear signal processing. Furthermore, Nielsen *et al.* demonstrated efficient four-wave mixing driven by plasmonic nanofocusing on this platform (Fig. 7e), confirming the significant advantage of geometrically induced compression for enhancing nonlinear optical processes^[17].

3 Hybrid in-plane and out-of-plane compression

Hybrid in-plane and out-of-plane compression refers to the simultaneous compression of optical modes in both the in-plane (lateral) and out-of-plane (axial) directions within a photonic structure. Structurally, hybrid in-plane-out-of-plane compression is realized by combining an axially confined resonant unit with a laterally engineered mode-shaping component. Out-of-plane compression is typically achieved through nanogaps, multilayer interfaces, metal-dielectric-metal cavities, or guided-

mode boundary conditions, which concentrate electromagnetic fields along the normal direction. In contrast, in-plane compression is introduced through cavity geometry design, photonic-crystal confinement, antenna coupling, symmetry breaking, or disorder engineering, which suppress lateral spreading and reshape the in-plane mode distribution. Representative implementations include plasmonic nanogap cavities^[74], hybrid plasmonic-photonic cavities^[75], disorder-modulated plasmonic structures^[76], geometry-confined plasmonic structures^[18], tapered-waveguide compression structures^[16], and polaritonic heterostructures based on van der Waals materials^[31]. Compared with single compression mechanisms, hybrid in-plane-out-of-plane compression preserves mode coupling and transport properties while enabling orders-of-magnitude enhancement of confined fields and substantial reduction of the effective mode volume, thereby greatly strengthening light-matter interactions. Owing to these advantages, this mechanism shows significant potential for applications in nonlinear optical communication, surface-enhanced infrared absorption (SEIRA), and emission control.

In practical applications, the six basic compression mechanisms exhibit distinct strengths and limitations. Among the out-of-plane mechanisms, surface plasmon polaritons (SPPs) provide strong field enhancement, deep subwavelength compression, and good compatibility with integrated photonic platforms, but they usually suffer from metallic loss and limited control over lateral spreading. SPhPs generally offer lower loss and stronger spectral selectivity than SPPs, and they can support highly confined infrared modes, but their operating bands are restricted by the material phonon resonances and their material platforms are less general. Waveguide modes, by contrast, are advantageous for low-loss transport, efficient coupling, and large-scale integration, yet their field compression is usually weaker than that of plasmonic or phonon-polaritonic modes. Among the in-plane mechanisms, disorder-induced Anderson compression is effective for suppressing lateral transport and forming strongly confined localized modes, but its modal properties are sensitive to disorder configuration and are therefore less deterministic in design and fabrication. Band-gap-induced defect-state compression provides better spectral selectivity and more controllable mode positioning, but it is often narrowband and sensitive to structural perturbation. Geometry-induced compression offers strong field confinement and clear spatial control of hot-spots, which is advantageous for local enhancement and mode shaping, yet its active region is usually limited in size and may be less suitable for applications requiring large-area uniform enhancement.

The design of hybrid compression is governed by the dominant physical quantity to be controlled, such as field intensity, spatial confinement, spectral selectivity, or modal transport. Different compression mechanisms act on distinct physical degrees of freedom, and hybrid compression arises from their coordinated integration within a single structure. For applications requiring

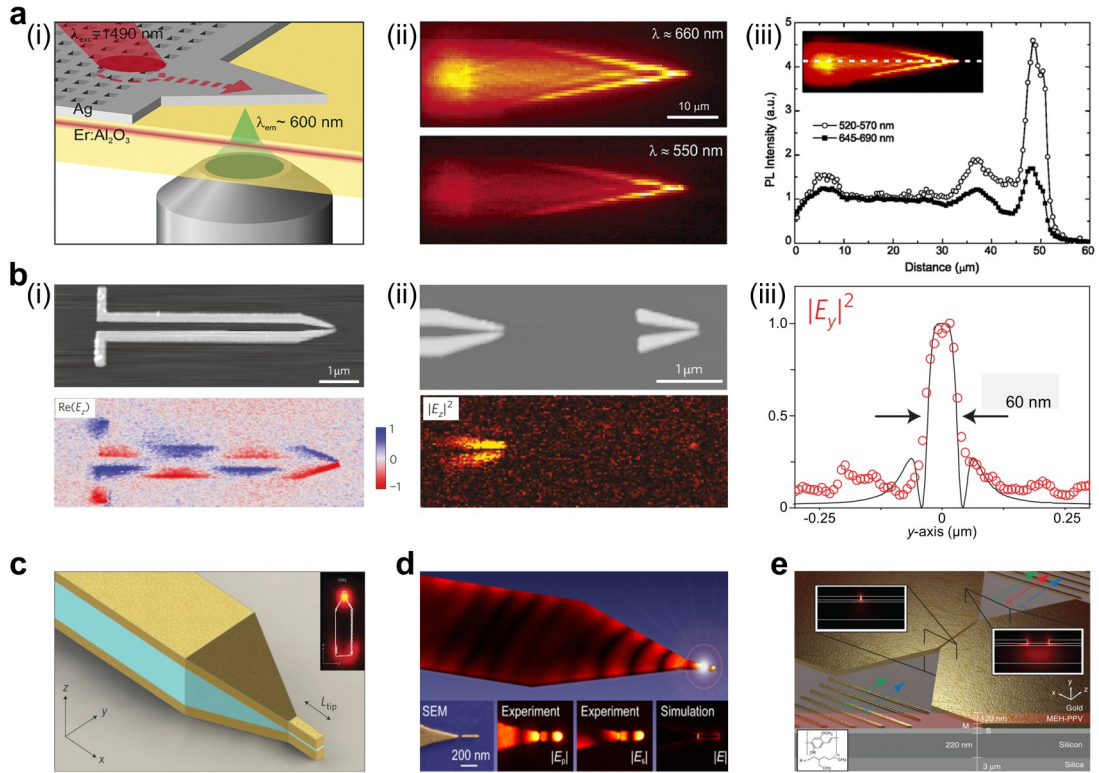


图7 几何诱导压缩:(a) (i)锥形等离子激元波导中的上转换发光成像原理($\lambda = 1.49 \mu\text{m}$)。(ii)空间分辨的光致发光分布。(iii)沿锥形波导轴向的截面发光强度分布曲线^[18];(b) (i)锥形双线传输线的形貌及其实验测得的近场图像 $\text{Re}(E_z)$ 。(ii)锥形传输线与孤立锥形结构的对比实验。(iii)锥尖处焦斑的线剖面分布($\lambda = 9.3 \mu\text{m}$)^[70];(c)三维MIM(金属-绝缘体-金属)纳米等离子光压缩器示意图(TPPL共焦测量;830 nm, 120 fs 脉冲, 54 MHz, 210 mW)^[71];(d)锥形条带波导中的纳米聚焦效应^[72];(e)硅-有机杂化等离子激元间隙波导结构示意图^[17]。

Fig. 7 Geometry-induced compression: (a) (i) Principle of upconversion luminescence imaging in a tapered plasmonic waveguide ($\lambda = 1.49 \mu\text{m}$). (ii) Spatially resolved photoluminescence distribution. (iii) Cross-sectional luminescence profiles along the tapered waveguide axis^[18]; (b) (i) Topography of a tapered two-wire transmission line and experimental near-field image showing $\text{Re}(E_z)$. (ii) Experiment comparing a tapered transmission line with an isolated taper. (iii) Line profile of the focal spot at the taper apex ($\lambda = 9.3 \mu\text{m}$)^[70]; (c) Schematic illustration of the three-dimensional MIM nanoplasmic photon compressor (TPPL confocal measurement; 830 nm, 120 fs pulses, 54 MHz, 210 mW)^[71]; (d), Nanofocusing effect in a tapered stripe waveguide^[72]. e, Schematic of a hybrid silicon-organic plasmonic gap waveguide^[17].

strong local field enhancement, such as SEIRA and nonlinear optics, out-of-plane mechanisms provide the dominant contribution and are combined with in-plane confinement to restrict lateral spreading. In this regime, SPPs modes coupled with geometry-induced or disorder-induced in-plane compression enable high field intensity within a confined interaction region. Representative implementations include nanogap plasmonic structures combined with anisotropic in-plane geometries, which simultaneously enhance molecular signals and improve spatial selectivity^[6]. When spectral selectivity and low-loss transport are prioritized, waveguide modes serve as the primary component and are combined with bandgap-induced defect-state compression. This configuration enables simultaneous control of mode selection, field localization, and propagation, and is particularly relevant for infrared photodetection and integrated photonic sys-

tems^[39]. For emission control, strong light-matter interaction must be achieved together with controlled radiation properties. This is realized by combining strongly confined plasmonic modes with photonic-crystal defect modes, where the former provides large enhancement and the latter governs spectral response and radiation characteristics. For example, anisotropic gap-plasmon nanocavities enable polarization-selective emission through dipole-selective coupling^[74], while hybrid photonic-plasmonic cavities combine ultrasmall mode volumes with spectral confinement, allowing simultaneous control of emission enhancement and linewidth^[77].

4 Applications of infrared Field compression

Optical field compression confines electromagnetic

modes within subwavelength volumes through spatial constraints. Its physical effects mainly manifest in three aspects. First, strong mode-volume compression concentrates electromagnetic fields within subwavelength regions. This leads to pronounced field enhancement and facilitates optical absorption, scattering, and nonlinear responses. Second, the LDOS is modified, enabling modulation of spontaneous emission rates, radiation efficiency, and emission directivity. Third, structural geometry determines the spatial distribution and spectral response of optical modes, enabling selective enhancement or suppression within specific spectral bands. These physical effects provide the foundation for diverse applications of infrared optical mode volume compression, including infrared detection, infrared spectroscopy and molecular sensing, as well as nanoscale characterization, as shown in Fig. 8.

In infrared photodetection, the key advantage of optical compression structures lies in overcoming the conventional trade-offs among responsivity, bandwidth, and dark current^[78]. Hu *et al.* showed in their intriguing theory of dark-current mechanisms that the dark current in infrared photodetectors is closely related to the junction configuration of the photoactive material and the thickness of the absorber layer^[79]. Optical compression structures compress the incident optical energy into a smaller effective absorption volume, thereby enhancing light absorption and photoresponse and enabling efficient photodetection even with thinner absorber layers. By integrating waveguide-based compression structures with low-dimensional materials such as PdSe₂^[80], graphene^[81], and colloidal quantum dots^[82], significant progress has been achieved in improving detection efficiency, extending the operating spectral range, and enhancing spectral resolution. Additionally, the integration of two-dimensional material heterostructures with optical compression structures has further enhanced infrared photodetection performance. For example, GaSe/Si metasurface heterostructures enable tunable narrowband infrared up-conversion detection in the telecommunication band^[83]. MoS₂/WSe₂ heterostructures integrated with plasmonic metasurfaces achieve high-responsivity near-infrared detection around 1550 nm at room temperature^[84]. Black phosphorus natural heterojunction photodetectors integrated with subwavelength compression structures exhibit enhanced infrared detection performance^[85]. In recent years, SPPs compression structures have further advanced infrared detection, particularly in polarization-sensitive detection and multidimensional imaging. Coupling plasmonic metamaterial absorbers with tellurium nanoribbons enables polarization detection with a polarization ratio up to 2.5×10^4 at room temperature. This structure also provides high sensitivity to polarization angle, significantly improving polarization detection accuracy^[86]. In addition, ferroelectric super-domains modulate confined optical fields to enable multichannel infrared imaging detector arrays, enhancing edge recognition capability and multidimensional information sensing^[87]. The pioneering theory of localized field modulation proposed by Hu *et*

al. opens new opportunities for the integration and functional monolithic implementation of optical compression structures with photoconversion devices, thereby enabling enhanced light-matter interaction and efficient photoelectric conversion^[47, 88]. These advances indicate that optical compression is driving infrared detection from conventional intensity-based measurements toward vectorial and multidimensional optical information sensing^[89, 90].

In infrared spectroscopy and molecular sensing, optical compression structures significantly increase molecular vibrational absorption cross-sections through strong near-field enhancement, amplifying weak signals by several orders of magnitude. Metallic nanoantennas, through confined SPPs, generate highly confined hot spots at tips or nanogaps, enabling sensitive detection of molecular monolayers^[5, 6]. In addition, Paggi *et al.* designed an overcoupled resonant cavity that enables direct enhancement of molecular fingerprint signals over a broad spectral range of 5-10 μm ^[91]. High-Q confined modes based on metasurface Fano resonances further improve spectral contrast and detection sensitivity^[92]. These developments indicate that confined optical fields are driving infrared molecular sensing toward higher sensitivity and broader spectral coverage.

In emission and radiation, optical compression structures enhance light emission by increasing the LDOS. For example, defect photonic-crystal microcavities, characterized by high quality factors and ultrasmall mode volumes, produce strong Purcell enhancement. Compression significantly improves the radiation efficiency of emitters such as quantum dots^[93, 94]. In disordered systems, AL creates spatially confined modes through multiple scattering and coherent interference, enabling high-Q random cavities and stable narrow-linewidth emission^[95]. Furthermore, plasmonic nanocavities and optical antennas accelerate spontaneous emission through subwavelength field compression^[96, 97].

In nanoscale characterization, strongly confined structures generate subwavelength electromagnetic hot spots using metallic tips or plasmonic probes, compressing optical fields to tens-of-nanometer scales and thereby enhancing near-field light-matter interactions. Based on this principle, techniques such as scattering-type scanning near-field optical microscopy (s-SNOM) and photo-thermal-induced resonance (AFM-IR) overcome the diffraction limit and enable nanoscale-resolution infrared spectroscopic imaging. These methods have been widely applied in polariton imaging^[98] and structural analysis of single protein molecules.

5 Conclusion and Outlook

This review examines infrared optical compression from the perspective of axial symmetry and systematically summarizes the main mechanisms for realizing confined infrared optical fields. Different compression mechanisms are compared in terms of their compression scales and field distribution characteristics. In general, they compress electromagnetic fields into subwavelength re-

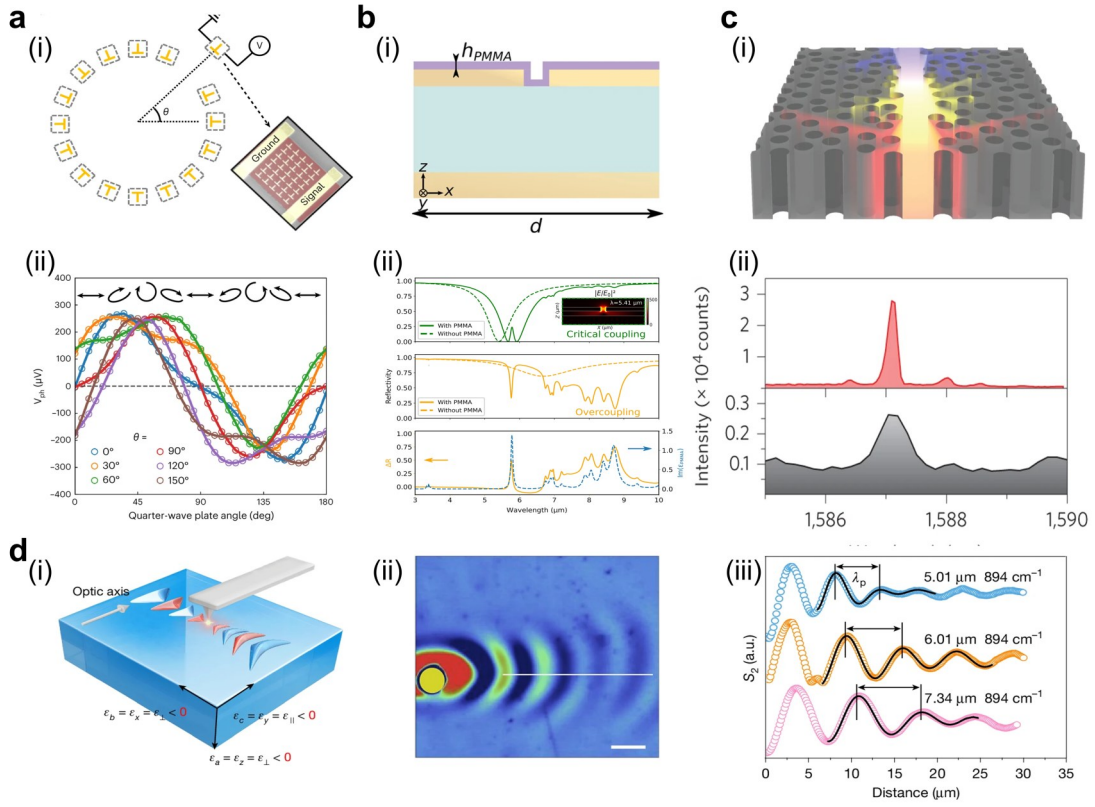


图8 光学压缩的应用:(a) (i) 等离激元纳米结构中取向可控的偏振依赖性示意图。(ii) 不同 θ 条件下测得的偏振依赖光电电压响应^[90];(b) (i) 用于宽带表面增强红外吸收 SEIRA 的过耦合谐振器示意图。(ii) 在临界耦合与过耦合条件下,用于 PMMA 的超表面 SEIRA 反射谱对比^[91];(c) (i) 由安德森局域模构成的无序光子晶体波导中随机激光的示意图。(ii) 在激发功率为 240 μW 和 600 μW 条件下测得的光致发光光谱^[95];(d) (i) 散射型扫描近场光学显微镜 (s-SNOM) 示意图。(ii) 声子极化激元的近场实验图像。(iii) 沿白色实线提取的极化激元场分布线扫结果^[98]。


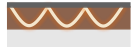




Fig. 8 Applications of optical compression: (a) (i) Schematic illustration of orientation-controlled polarization dependence in plasmonic nanostructures. (ii) Measured polarization-dependent photovoltages at different θ ^[90]; (b) (i) Schematic of an overcoupled resonator for broadband surface-enhanced infrared absorption (SEIRA). (ii) Reflectivity spectra of a metasurface for SEIRA of PMMA under critical-coupling and overcoupling conditions^[91]; (c) (i) Schematic illustration of random lasing in a disordered photonic crystal waveguide formed by Anderson-localized modes. (ii) Photoluminescence spectra measured at excitation powers of 240 μW and 600 μW ^[95]; (d) (i) Schematic of scattering-type scanning near-field optical microscopy (s-SNOM). (ii) Experimental near-field image of phonon polaritons. (iii) Line scans of the measured polariton fields along the solid white line^[98].

gions, thereby enhancing sub-wavelength electric field intensity and reducing the effective mode volume. Infrared optical compression has already shown considerable potential in applications including infrared detection, surface-enhanced absorption, nonlinear optics, and emission control.

Building on these advances, future research on infrared optical compression is expected to evolve from optimizing individual compression mechanisms toward the synergistic design of multiple compression mechanisms^[111]. For example, combining plasmonic and phonon-polaritonic modes within a single architecture may enable multidimensional control of optical fields across a broader spectral range through multi-mechanism coupling^[112]. With the development of emerging polaritonic materials, anisotropic two-dimensional crystals, and low-

loss photonic structures, the material and structural platforms supporting high-quality infrared confined modes continue to expand. Meanwhile advances in heterogeneous integration and band engineering enable control of the interfacial dielectric environment and electronic band structure, providing opportunities for coordinated design of compression scale, modal dispersion, and quality factor. In addition, external-field-driven modulation mechanisms, including electrical, thermal, or phase-change control, may offer opportunities for dynamically tuning the spectral positions and spatial distributions of confined modes. With the continued integration of advanced materials, structural design, and dispersion engineering, infrared optical compression structures are expected to enable stronger subwavelength field compression and improved control of modal properties. These advances pro-

Tab. 1 Comparison of Infrared Field Compression Mechanisms and Performance

Mechanism	Advantages	Typical application	Key metric*	Ref.
 SPPs	Strong field enhancement	Infrared photodetection	$R \approx 0.5 \text{ A/W}$ $\lambda \approx 0.8\text{--}1.55 \mu\text{m}$	[78]
	Subwavelength compression	Molecular sensing	$E \approx 10^2\text{--}10^3$ $\lambda \approx 6\text{--}13 \mu\text{m}$	[99]
	Good integrability	Emission manipulation	$Q \approx 15.7$ $\lambda \approx 3.96 \mu\text{m}$	[100]
 SPhPs	Low loss	Infrared photodetection	$R \approx 65 \text{ A/W}$ $\lambda \approx 6.7 \mu\text{m}$	[101]
	Strong compression	Molecular sensing	$E \approx 5$ $\lambda \approx 6.63 \mu\text{m}$	[102]
	High spectral selectivity	Emission manipulation	$Q \approx 101$ $\lambda \approx 10.9 \mu\text{m}$	[103]
 Waveguides	Low loss	Infrared photodetection	$R \approx 0.4 \text{ A/W}$ $\lambda \approx 1.55 \mu\text{m}$	[41]
	Long propagation length	Molecular sensing	$E \approx 6.15$ $\lambda \approx 7.7 \mu\text{m}$	[104]
	High coupling efficiency	Emission manipulation	$Q \approx 10^2\text{--}10^4$ $\lambda \approx 8.2 \mu\text{m}$	[105]
 Disorder-induced compression	Low loss	Infrared photodetection	$R \approx 0.22 \text{ A/W}$ $\lambda \approx 1.55 \mu\text{m}$	[106]
	Strong in-plane localization	Molecular sensing	/	/
		Emission manipulation	$Q \approx 10^3\text{--}10^4$ $\lambda \approx 0.96 \mu\text{m}$	[2]
 Bandgap-induced defect-state compression	High Q factor	Infrared photodetection	$R \approx 0.12 \text{ A/W}$ $\lambda \approx 1.55 \mu\text{m}$	[107]
	Controllable modes	Molecular sensing	$E \approx 20$ $\lambda \approx 0.78 \mu\text{m}$	[108]
	Strong spectral selectivity	Emission manipulation	$Q \approx 4.5 \times 10^4$ $\lambda \approx 1.58 \mu\text{m}$	[60]
 Geometry-induced compression		Infrared photodetection	$R \approx 11.5 \text{ A/W}$ $\lambda \approx 20 \mu\text{m}$	[109]
	Strong local enhancement	Molecular sensing	$E \approx 300$ $\lambda \approx 5.7 \mu\text{m}$	[91]
	Deterministic hotspot control	Emission manipulation	$E \approx 140$ $\lambda \approx 1.42 \mu\text{m}$	[72]
	High spatial selectivity	nanoscale characterization	$E \approx 10^2\text{--}10^3$ broadband	[110]

* denotes responsivity, denotes enhancement factor, denotes the operating wavelength, denotes the quality factor.

vide new physical platforms for studying strong light-matter interactions and may open broader opportunities in quantum photonics, infrared photoelectric detection^[113, 114], high-sensitivity sensing^[115, 116], and on-chip photonic devices^[117].

References

[1] Moore S L, Lee H Y, Rivera N, et al. Van der Waals waveguide quantum electrodynamics probed by infrared nano-photolu-

minescence[J]. *Nature Photonics*, 2025, 19(8): 833-839.

[2] Sapienza L, Thyrrstrup H, Stobbe S, et al. Cavity quantum electrodynamics with Anderson-localized modes [J]. *Science*, 2010, 327(5971): 1352-1355.

[3] Sauvan C, Hugonin J P, Maksymov I S, et al. Theory of the spontaneous optical emission of nanosize photonic and plasmon resonators [J]. *Physical Review Letters*, 2013, 110 (23) : 237401.

[4] Jiang F, Shi M, Zhou J, et al. Integrated photonic structure enhanced infrared photodetectors [J]. *Advanced Photonics Research*, 2021, 2(9): 2000187.

- [5] Liu N, Tang M L, Hentschel M, et al. Nanoantenna-enhanced gas sensing in a single tailored nanofocus[J]. *Nature Materials*, 2011, 10(8): 631-636.
- [6] Neubrech F, Pucci A, Cornelius T W, et al. Resonant plasmonic and vibrational coupling in a tailored nanoantenna for infrared detection[J]. *Physical Review Letters*, 2008, 101(15): 157403.
- [7] Timmer D, Gittinger M, Quenzel T, et al. Ultrafast transition from coherent to incoherent polariton nonlinearities in a hybrid 1L-WS₂/plasmon structure[J]. *Nature Nanotechnology*, 2026: 1-7.
- [8] Lin H, Luo Z, Gu T, et al. Mid-infrared integrated photonics on silicon: a perspective [J]. *Nanophotonics*, 2017, 7(2): 393-420.
- [9] Garcia-Vidal F J, Fernández-Domínguez A I, Martín-Moreno L, et al. Spoof surface plasmon photonics[J]. *Reviews of Modern Physics*, 2022, 94(2): 025004.
- [10] Basov D N, Fogler M M, García de Abajo F J. Polaritons in van der Waals materials [J]. *Science*, 2016, 354(6309): aag1992.
- [11] Qi M, Lidorikis E, Rakich P T, et al. A three-dimensional optical photonic crystal with designed point defects [J]. *Nature*, 2004, 429(6991): 538-542.
- [12] Chabanov A A, Stoytchev M, Genack A Z. Statistical signatures of photon localization [J]. *Nature*, 2000, 404(6780): 850-853.
- [13] Jahani S, Kim S, Atkinson J, et al. Controlling evanescent waves using silicon photonic all-dielectric metamaterials for dense integration [J]. *Nature Communications*, 2018, 9(1): 1893.
- [14] Segev M, Silberberg Y, Christodoulides D N. Anderson localization of light[J]. *Nature Photonics*, 2013, 7(3): 197-204.
- [15] Painter O, Lee R K, Scherer A, et al. Two-dimensional photonic band-gap defect mode laser [J]. *Science*, 1999, 284(5421): 1819-1821.
- [16] Stockman M I. Nanofocusing of optical energy in tapered plasmonic waveguides [J]. *Physical Review Letters*, 2004, 93(13): 137404.
- [17] Nielsen M P, Shi X, Dichtl P, et al. Giant nonlinear response at a plasmonic nanofocus drives efficient four-wave mixing [J]. *Science*, 2017, 358(6367): 1179-1181.
- [18] Verhagen E, Kuipers L, Polman A. Enhanced nonlinear optical effects with a tapered plasmonic waveguide [J]. *Nano Letters*, 2007, 7(2): 334-337.
- [19] Barnes W L, Dereux A, Ebbesen T W. Surface plasmon sub-wavelength optics[J]. *Nature*, 2003, 424(6950): 824-830.
- [20] Maier S A. *Plasmonics: fundamentals and applications* [M]. New York: Springer, 2007.
- [21] Sobhani A, Knight M W, Wang Y, et al. Narrowband photodetection in the near-infrared with a plasmon-induced hot electron device[J]. *Nature Communications*, 2013, 4(1): 1643.
- [22] Alcaraz Iranzo D, Nanot S, Dias E J C, et al. Probing the ultimate plasmon confinement limits with a van der Waals heterostructure[J]. *Science*, 2018, 360(6386): 291-295.
- [23] Fang Z, Liu Z, Wang Y, et al. Graphene-antenna sandwich photodetector[J]. *Nano Letters*, 2012, 12(7): 3808-3813.
- [24] Wei J, Li Y, Wang L, et al. Zero-bias mid-infrared graphene photodetectors with bulk photoresponse and calibration-free polarization detection[J]. *Nature Communications*, 2020, 11(1): 6404.
- [25] Wei J, Xu C, Dong B, et al. Mid-infrared semimetal polarization detectors with configurable polarity transition [J]. *Nature Photonics*, 2021, 15(8): 614-621.
- [26] Wisch J A, Green K A, Lemay A C, et al. Plasmon-enhanced ultralow-threshold solid-state triplet fusion upconversion[J]. *Nature Photonics*, 2025: 1-7.
- [27] Lemasters R, Manjare M, Freeman R, et al. Non-thermal emission in gap-mode plasmon photoluminescence [J]. *Nature Communications*, 2024, 15(1): 4468.
- [28] Zhong J H, Vogelsang J, Yi J M, et al. Nonlinear plasmon-exciton coupling enhances sum-frequency generation from a hybrid metal/semiconductor nanostructure [J]. *Nature Communications*, 2020, 11(1): 1464.
- [29] Wang X, Huang S C, Hu S, et al. Fundamental understanding and applications of plasmon-enhanced Raman spectroscopy [J]. *Nature Reviews Physics*, 2020, 2(5): 253-271.
- [30] Lemcoff N, Nechmad N B, Eivigi O, et al. Plasmonic visible-near infrared photothermal activation of olefin metathesis enabling photoresponsive materials [J]. *Nature Chemistry*, 2023, 15(4): 475-482.
- [31] Dai S, Fei Z, Ma Q, et al. Tunable phonon polaritons in atomically thin van der Waals crystals of boron nitride [J]. *Science*, 2014, 343(6175): 1125-1129.
- [32] Agranovich V M, Mills D L, eds. *Surface polaritons* [M]. Amsterdam; North-Holland, 1982.
- [33] Ma W, Alonso-González P, Li S, et al. In-plane anisotropic and ultra-low-loss polaritons in a natural van der Waals crystal [J]. *Nature*, 2018, 562(7728): 557-562.
- [34] Zhao Y, Chen J, Xue M, et al. Ultralow-loss phonon polaritons in the isotope-enriched α -MoO₃ [J]. *Nano Letters*, 2022, 22(24): 10208-10215.
- [35] Pan Z, Lu G, Li X, et al. Remarkable heat conduction mediated by non-equilibrium phonon polaritons [J]. *Nature*, 2023, 623(7986): 307-312.
- [36] Guo Q, Esin I, Li C, et al. Hyperbolic phonon-polariton electroluminescence in 2D heterostructures [J]. *Nature*, 2025, 639(8056): 915-921.
- [37] Hutchins W, Zare S, Hirt D M, et al. Ultrafast evanescent heat transfer across solid interfaces via hyperbolic phonon-polariton modes in hexagonal boron nitride [J]. *Nature Materials*, 2025, 24(5): 698-706.
- [38] Smirnova D, Komissarenko F, Vakulenko A, et al. Polaritonic states trapped by topological defects [J]. *Nature Communications*, 2024, 15(1): 6355.
- [39] Wang X, Cheng Z, Xu K, et al. High-responsivity graphene/silicon-heterostructure waveguide photodetectors [J]. *Nature Photonics*, 2013, 7(11): 888-891.
- [40] Gan X, Shiue R J, Gao Y, et al. Chip-integrated ultrafast graphene photodetector with high responsivity [J]. *Nature Photonics*, 2013, 7(11): 883-887.
- [41] Guo J, Li J, Liu C, et al. High-performance silicon-graphene hybrid plasmonic waveguide photodetectors beyond 1.55 μm [J]. *Light: Science & Applications*, 2020, 9(1): 1-11.
- [42] Flóry N, Ma P, Salamin Y, et al. Waveguide-integrated van der Waals heterostructure photodetector at telecom wavelengths with high speed and high responsivity [J]. *Nature Nanotechnology*, 2020, 15(2): 118-124.
- [43] Li Q, Yi Q, Sun A, et al. Ultra-broadband near-to mid-infrared electro-optic modulator on thin-film lithium niobate [J]. *Nature Communications*, 2026.
- [44] Kuyken B, Ideguchi T, Holzner S, et al. An octave-spanning mid-infrared frequency comb generated in a silicon nanophotonic wire waveguide [J]. *Nature Communications*, 2015, 6(1): 6310.
- [45] Chen C, Yang Z, Wang T, et al. Ultra-broadband all-optical nonlinear activation function enabled by MoTe₂/optical wave-

- guide integrated devices[J]. *Nature Communications*, 2024, 15 (1): 9047.
- [46] Álvarez-Pérez G, Hu H, Huang F, et al. Ultrahigh free-electron Kerr nonlinearity in all-semiconductor waveguides for all-optical nonlinear modulation of mid-infrared light[J]. *npj Nanophotonics*, 2025, 2(1): 33.
- [47] He T, Ma H, Wang Z, et al. On-chip optoelectronic logic gates operating in the telecom band[J]. *Nature Photonics*, 2024, 18 (1): 60-67.
- [48] Anderson P W. Absence of diffusion in certain random lattices [J]. *Physical Review*, 1958, 109(5): 1492.
- [49] Abrahams E, Anderson P W, Licciardello D C, et al. Scaling theory of localization: Absence of quantum diffusion in two dimensions[J]. *Physical Review Letters*, 1979, 42(10): 673.
- [50] John S. Strong localization of photons in certain disordered dielectric superlattices [J]. *Physical Review Letters*, 1987, 58 (23): 2486.
- [51] Hu H, Strybulevych A, Page J H, et al. Localization of ultrasound in a three-dimensional elastic network[J]. *Nature Physics*, 2008, 4(12): 945-948.
- [52] Bertolotti J, Gottardo S, Wiersma D S, et al. Optical necklace states in Anderson localized 1D systems [J]. *Physical Review Letters*, 2005, 94(11): 113903.
- [53] Schwartz T, Bartal G, Fishman S, et al. Transport and Anderson localization in disordered two-dimensional photonic lattices [J]. *Nature*, 2007, 446(7131): 52-55.
- [54] Levi L, Rechtsman M, Freedman B, et al. Disorder-enhanced transport in photonic quasicrystals [J]. *Science*, 2011, 332 (6037): 1541-1544.
- [55] Pertsch T, Peschel U, Kobelke J, et al. Nonlinearity and disorder in fiber arrays[J]. *Physical Review Letters*, 2004, 93(5): 053901.
- [56] Abaie B, Mobini E, Karbasi S, et al. Random lasing in an Anderson localizing optical fiber [J]. *Light: Science & Applications*, 2017, 6(8): e17041
- [57] Karbasi S, Frazier R J, Koch K W, et al. Image transport through a disordered optical fibre mediated by transverse Anderson localization [J]. *Nature Communications*, 2014, 5(1): 3362.
- [58] Arregui G, Ng R C, Albrechtsen M, et al. Cavity optomechanics with Anderson-localized optical modes[J]. *Physical Review Letters*, 2023, 130(4): 043802.
- [59] Noda S, Chutinan A, Imada M. Trapping and emission of photons by a single defect in a photonic bandgap structure[J]. *Nature*, 2000, 407(6804): 608-610.
- [60] Akahane Y, Asano T, Song B S, et al. High-Q photonic nanocavity in a two-dimensional photonic crystal[J]. *Nature*, 2003, 425(6961): 944-947.
- [61] Song B S, Noda S, Asano T, et al. Ultra-high-Q photonic double-heterostructure nanocavity [J]. *Nature Materials*, 2005, 4 (3): 207-210.
- [62] Englund D, Fattal D, Waks E, et al. Controlling the Spontaneous Emission Rate of Single Quantum Dots in a Two-Dimensional Photonic Crystal[J]. *Physical Review Letters*, 2005, 95 (1): 013904.
- [63] Yoshie T, Scherer A, Hendrickson J, et al. Vacuum Rabi splitting with a single quantum dot in a photonic crystal nanocavity [J]. *Nature*, 2004, 432(7014): 200-203.
- [64] Noh J, Benalcazar W A, Huang S, et al. Topological protection of photonic mid-gap defect modes [J]. *Nature Photonics*, 2018, 12(7): 408-415.
- [65] Zhu B, Hean K, Wong S, et al. Topological photonic crystal fiber[J]. *Science Advances*, 2025, 11(46): eady1476.
- [66] Rong K, Wang B, Reuven A, et al. Photonic Rashba effect from quantum emitters mediated by a Berry-phase defective photonic crystal [J]. *Nature Nanotechnology*, 2020, 15 (11) : 927-933.
- [67] Vaidya S, Benalcazar W A, Cerjan A, et al. Point-defect-localized bound states in the continuum in photonic crystals and structured fibers [J]. *Physical Review Letters*, 2021, 127 (2) : 023605.
- [68] Jackson J D. *Classical electrodynamics*[M]. 3rd ed. New York: John Wiley & Sons, 1998.
- [69] Deng K, Xiao Y, Guo D, et al. High transmission efficiency long-wave infrared multispectral modulation array based on nanogap engineering [J]. *Infrared Physics & Technology*, 2024, 142: 105559.
- [70] Schnell M, Alonso-Gonzalez P, Arzubiaiga L, et al. Nanofocusing of mid-infrared energy with tapered transmission lines [J]. *Nature Photonics*, 2011, 5(5): 283-287.
- [71] Choo H, Kim M K, Staffaroni M, et al. Nanofocusing in a metal-insulator-metal gap plasmon waveguide with a three-dimensional linear taper [J]. *Nature Photonics*, 2012, 6 (12) : 838-844.
- [72] Zenin V A, Andryieuski A, Malureanu R, et al. Boosting local field enhancement by on-chip nanofocusing and impedance-matched plasmonic antennas[J]. *Nano letters*, 2015, 15(12): 8148-8154.
- [73] Nielsen M P, Lafone L, Rakovich A, et al. Adiabatic nanofocusing in hybrid gap plasmon waveguides on the silicon-on-insulator platform[J]. *Nano letters*, 2016, 16(2): 1410-1414.
- [74] Xu K, Zou Z, Li W, et al. Strong linearly polarized light emission by coupling out-of-plane exciton to anisotropic gap plasmon nanocavity[J]. *Nano Letters*, 2024, 24(12): 3647-3653.
- [75] Barreda Á, Mercadé L, Zapata-Herrera M, et al. Hybrid photonic-plasmonic cavity design for very large Purcell factors at telecommunication wavelengths [J]. *Physical Review Applied*, 2022, 18(4): 044066.
- [76] Shi W B, Liu L Z, Peng R, et al. Strong localization of surface plasmon polaritons with engineered disorder [J]. *Nano letters*, 2018, 18(3): 1896-1902.
- [77] Gong Y, Vuckovic J. Photonic-plasmonic hybrid nanocavity for strong light-matter interaction [J]. *Nano Letters*, 2014, 14(8) : 4429-4434
- [78] Ma P, Salamin Y, Baeuerle B, et al. Plasmonically enhanced graphene photodetector featuring 100 Gbit/s data reception, high responsivity, and compact size [J]. *ACS Photonics*, 2018, 6(1): 154-161
- [79] Chen Y, Wang Y, Wang Z, et al. Unipolar barrier photodetectors based on van der Waals heterostructures [J]. *Nature Electronics*, 2021, 4(5): 357-363.
- [80] Wu J, Ma H, Zhong C, et al. Waveguide-Integrated PdSe₂ Photodetector over a Broad Infrared Wavelength Range [J]. *Nano Letters*, 2022, 22(16): 6816-6824.
- [81] Goldstein J, Lin H, Deckoff-Jones S, et al. Waveguide-integrated mid-infrared photodetection using graphene on a scalable chalcogenide glass platform [J]. *Nature Communications*, 2022, 13(1): 3915.
- [82] Grotevent M J, Yakunin S, Bachmann D, et al. Integrated photodetectors for compact Fourier-transform waveguide spectrometers [J]. *Nature Photonics*, 2022, 16(12): 875-882.
- [83] Ye Y, Hu X, Li Y, et al. Infrared upconversion detection based on two-dimensional material/silicon tunable metasurface heterostructures for telecommunication [J]. *Applied Physics Letters*, 2025, 126(11): 111102.
- [84] Zhang Q, et al. Anapole-state-enhanced two-dimensional hetero-

- structure photodetector for near-infrared detection [J]. *Nature Communications*, 2026, 17, 2907.
- [85] Luo M, Ge H, Liu S, et al. Sub-wavelength optical modulation of step-size varying infrared photodetectors[J]. *Infrared Physics & Technology*, 2025, 145: 105668.
- [86] Dai M, Wang C, Qiang B, et al. On-chip mid-infrared photothermoelectric detectors for full-Stokes detection [J]. *Nature Communications*, 2022, 13(1): 4560.
- [87] Dai M, Wang C, Qiang B, et al. Long-wave infrared photothermoelectric detectors with ultrahigh polarization sensitivity [J]. *Nature Communications*, 2023, 14(1): 3421.
- [88] Luo M, Zhi Z, Liu A, et al. Nonlinear infrared photocurrent driven by Lifshitz transition [J]. *Infrared Physics & Technology*, 2025, 136: 106244
- [89] Guo J, Gu S, Lin L, et al. Type-printable photodetector arrays for multichannel meta-infrared imaging[J]. *Nature Communications*, 2024, 15(1): 5193.
- [90] Wei J, Chen Y, Li Y, et al. Geometric filterless photodetectors for mid-infrared spin light[J]. *Nature Photonics*, 2023, 17(2): 171-178.
- [91] Paggi L, Fabas A, El Ouazzani H, et al. Over-coupled resonator for broadband surface enhanced infrared absorption (SEIRA) [J]. *Nature Communications*, 2023, 14(1): 4814.
- [92] Wu C, Khanikaev A B, Adato R, et al. Fano-resonant asymmetric metamaterials for ultrasensitive spectroscopy and identification of molecular monolayers[J]. *Nature Materials*, 2012, 11(1): 69-75.
- [93] Aoki K, Guimard D, Nishioka M, et al. Coupling of quantum-dot light emission with a three-dimensional photonic-crystal nanocavity[J]. *Nature Photonics*, 2008, 2(11): 688-692.
- [94] Noda S, Fujita M, Asano T. Spontaneous-emission control by photonic crystals and nanocavities[J]. *Nature Photonics*, 2007, 1(8): 449-458.
- [95] Liu J, Garcia P D, Ek S, et al. Random nanolasing in the Anderson localized regime [J]. *Nature Nanotechnology*, 2014, 9(4): 285-289.
- [96] Freire-Fernández F, Park S M, Tan M J H, et al. Plasmonic lattice lasers [J]. *Nature Reviews Materials*, 2025, 10(8): 604-616.
- [97] Sidiropoulos T P H, Röder R, Geburt S, et al. Ultrafast plasmonic nanowire lasers near the surface plasmon frequency [J]. *Nature Physics*, 2014, 10(11): 870-876.
- [98] Liu L, Xiong L, Wang C, et al. Long-range hyperbolic polaritons on a non-hyperbolic crystal surface[J]. *Nature*, 2025, 644(8075): 76-82.
- [99] Yang X, Sun Z, Low T, et al. Nanomaterial-based plasmon-enhanced infrared spectroscopy[J]. *Advanced Materials*, 2018, 30(20): 1704896.
- [100] Li X, Li J, Moon J, et al. Experimental observation of Purcell-enhanced spontaneous emission in a single-mode plasmonic nanocavity[J]. *ACS Photonics*, 2024, 11(8): 3375-3380.
- [101] Castilla S, Vangelidis I, Pusapati V V, et al. Plasmonic antenna coupled to hyperbolic phonon-polaritons for sensitive and fast mid-infrared photodetection with graphene[J]. *Nature Communications*, 2020, 11(1): 4872.
- [102] Bylinkin A, Castilla S, Slipchenko T M, et al. On-chip phonon-enhanced IR near-field detection of molecular vibrations[J]. *Nature Communications*, 2024, 15(1): 8907.
- [103] Ma B, Huang Y, Zha W, et al. Narrowband diffuse thermal emitter based on surface phonon polaritons[J]. *Nanophotonics*, 2022, 11(17): 4115-4122.
- [104] Zhang D, Wang Y, Fu Q, et al. Ultra-high-enhancement-factor integrated long-wave infrared gas sensor based on the tapered sub-wavelength grating slot waveguide[J]. *Results in Physics*, 2023, 48: 106442.
- [105] Kazakov D, Letsou T P, Beiser M, et al. Active mid-infrared ring resonators[J]. *Nature Communications*, 2024, 15(1): 607.
- [106] Chen W, Zhang S, Wang C, et al. Enabling highly efficient infrared silicon photodetectors via disordered metasurfaces with upconversion nanoparticles [J]. *Science Advances*, 2025, 11(43): eadx7783.
- [107] Tian R, Gu L, Ji Y, et al. Black phosphorus photodetector enhanced by a planar photonic crystal cavity[J]. *ACS Photonics*, 2021, 8(10): 3104-3110.
- [108] Wu W, Zhang Z. Defect-engineered TiO₂ nanotube photonic crystals for the fabrication of near-infrared photoelectrochemical sensor [J]. *Journal of Materials Chemistry B*, 2017, 5(25): 4883-4889.
- [109] Cakmakyapan S, Lu P K, Navabi A, et al. Gold-patched graphene nano-strips for high-responsivity and ultrafast photodetection from the visible to infrared regime[J]. *Light: Science & Applications*, 2018, 7(1): 20.
- [110] Behr N, Raschke M B. Optical antenna properties of scanning probe tips: plasmonic light scattering, tip-sample coupling, and near-field enhancement [J]. *The Journal of Physical Chemistry C*, 2008, 112(10): 3766-3773.
- [111] Pei Y, Chen L, Jeon W, et al. Low-dimensional heat conduction in surface phonon polariton waveguide. *Nature Communications*, 2023, 14: 8242.
- [112] Dai S, Ma Q, Liu M K, et al. Graphene on hexagonal boron nitride as a tunable hyperbolic metamaterial[J]. *Nature Nanotechnology*, 2015, 10(8): 682-686.
- [113] Zhu L H, Duan S K, Chen M H, et al. Mid-wavelength infrared detector array based on black phosphorus ink thin film [J]. *Journal of Infrared and Millimeter Waves*, 2026: 1-11.
- [114] Li Q, He T, Zhang K, et al. Direct mapping and characterization of the surface local field in InGaAs/InP avalanche photodetectors [J]. *Infrared Physics & Technology*, 2022, 123: 104162.
- [115] Xu H, Xu Z, Ren Q, et al. Two-dimensional materials for integrated sensing[J]. *Nature Materials*, 2026: 1-15.
- [116] Shi X, Chen J, Wang J, et al. Refined lunar global chemistry mapping using farside ground truth information gathered by Chang'e-6[J]. *Nature Sensors*, 2026: 1-9.
- [117] Hu Z, Pan X, Ahammed R, et al. An all-in-one Hall rectenna with a bandwidth over 100 GHz[J]. *Nature Electronics*, 2026, 9(2): 140-151.

红外光场压缩

刘安娜^{1,2}, 刘书宁³, 焦守政^{1,2}, 高威⁴, 康乾龙¹, 罗敏¹, 孙慧盈⁵, 曹萌⁵,
葛浩楠¹, 王芳¹, 王鹏¹, 谢润章^{1*}

(1. 中国科学院上海技术物理研究所 红外科学与技术全国重点实验室, 上海 200083, 中国;

2. 中国科学院大学,北京 100049,中国;
3. 香港科技大学(广州)微电子学院,广州 511453,中国;
4. 同济大学 上海智能科学与技术研究院,上海 200092,中国;
5. 上海大学 材料科学与工程学院,上海 200444,中国)

摘要: 红外光场压缩为调控光学模式的色散特性与空间分布提供了一种有效途径。在自由空间或均匀介质中,红外传播模式通常受到衍射极限的限制,难以实现深亚波长尺度的场压缩。实现光场压缩通常需要对色散关系的调控以及结构几何参数的设计来实现。近年来,低维材料的发展以及微纳加工技术的进步,显著拓展了模式体积调控的物理实现路径。本文基于轴向对称性的角度,将红外光场压缩归纳为两种基本类型:面外压缩与面内压缩。面外压缩主要通过界面色散关系与边界条件的调控,在法向方向形成轴向压缩态,其典型实现机制包括表面等离激元(SPPs)、声子极化激元(SPhPs)以及波导模式等。面内压缩则通过无序诱导干涉、缺陷态或几何压缩等机制抑制模式的横向传播,从而实现光场在平面内的空间局域。本文系统比较了不同机制的物理起源及其对应的特征空间尺度,并综述了相关结构在红外光电探测、表面增强红外吸收以及发光调控等方面的研究进展。进一步讨论了面内与面外混合压缩在增强光场压缩和调控模式分布方面的潜力,并对未来研究方向进行了展望。

关键词: 光子结构;微纳光学;模式体积压缩;红外探测器;红外光源

中图分类号: O43

文献标识码: A